공학박사 학위논문

A Study on Fabrications of Super-Hydrophilic Nanostructures and Its Application

초친수 나노구조체의

형성과 그 응용

2020 년 2 월

서울대학교 대학원

재료공학부

김 민 성

A study on Fabrications of super-hydrophilic nanostructures and its application

초친수 나노구조체의 형성과 그 응용

지도교수 오 규 환

이 논문을 공학박사 학위논문으로 제출함

2019년 12월

서울대학교 대학원

재료공학부

김 민 성

김민성의 공학박사 학위논문을 인준함

2019년 12월

위 원 장 한 흥 남 (인)

부위원장 오 규 환 (인)

위 원 선 정 윤 (인)

위 원 문 명 운 (인)

위 원 Alfredo Alexander-Katz (인)

Abstract

Many of the creatures that exist in the nature have evolved their own functional surface to survive at surrounding environments and showing amazing functional performance. The fact was revealed, many of these surface have roughed structures from micro-scale to nano-scale. It gives lots of insights and ideas for many researchers. Hence we fabricated roughed surface to solve the existing challenging topics or problems like oil-water separation, self-cleaning surface, and anti-fogging.

Nanostructured cellulose fabric with an air-bubble enhanced anti-oil fouling property is introduced for quick oil-cleaning under a dry state. Anti-oil-fouling under a dry state was realized through two main features of the nanostructured, porous fabric: a low solid fraction with high-aspect-ratio nanostructures significantly increasing the retracting forces, and trapped multiscale air bubbles increasing the buoyancy and backpressure for an oil-layer rupture. The nanostructures were formed on cellulose-based rayon microfibers through selective etching with oxygen plasma, forming a nanoscale open-pore structure. Viscous crude oil fouled on a fabric under a dry state was cleaned by immersion into water owing to a higher water affinity of the rayon material and low solid fraction of the high-aspect-ratio nanostructures. Air bubbles trapped in dry porous fibers and nanostructures promote oil detachment from the fouled sites. The macroscale bubbles add buoyancy on top of the oil droplets, enhancing the oil receding at the oil-water-solid interface, whereas the relatively smaller microscale bubbles induce a backpressure underneath the oil droplets. The oil-proofing fabric was used for protecting underwater conductive sensors, allowing a robot fish to swim freely in oily water. In addition, we fabricated a highly adhesive hydrogel coating

layer on nanostructured polyethylene terephthalate (PET) polymer with high transparency and excellent underwater anti-oil-fouling properties. One-step selective oxygen plasma etching was adopted for the introduction of not only hydrophilicity, but also nanoscale roughness with high-aspect-ratio nanostructures (HARns) to enhance interfacial adhesion strength between the transparent hydrogel (polyacrylamide, PAAm) coating and PET substrate via mechanical interlocking. The transparency, which was initially reduced by the HARns, was improved by the hydrogel coating on the nanostructured PET because the refractive indices are well matched between the hydrogel and PET. Because the HARns formed on the PET appear as reflections on the hydrogel-coated surface, the PAAm-coated HARn PET was found to exhibit enhanced hydrophilicity and underwater oleophobicity, even for highly viscous crude oil, without aging. The PAAm-coated HARn PET was applied to an underwater optical device protector to provide anti-oil fouling in oily water. Its strong anti-oil fouling properties were well maintained after the polymer was physically damaged, allowing our it can be applied in wide range of application as protective windows for underwater cameras, optical sensors, and biosensors.

Additionally, as global oil production and transportation increase, oil spill probability also increases, and most these accidents occur at the ocean. Hence, most oil spill managements are operated in the maritime environment. However, recent oil cleanup studies have been getting focused development of oil-water separation efficiency using hydrophilic functional surfaces with few considering the real operation condition. Furthermore, functional surfaces can be easily fouled or damaged by precipitated minerals in seawater. Here, we introduce the mineral precipitation control using high aspect-ratio (AR) nanostructures, inspired by plants water-mineral transportation mechanism. These are explained from

experiments and numerical analysis with simple efflorescence model, that high AR nanostructures does not damage from the mineral crystallization even the hydrophilic nano-pillars were totally immersed in seawater. We also demonstrate robustness of underwater superoleophobicity by control the high AR.

Keyword : Hydrophilic, Anti-oil fouling, Anti-mineral fouling, Nanostructure, Oxygen plasma etching, hydrogel

Student Number : 2016-30194

Contents

List of Tables

List of Figures

Chapter 1. Introduction

1.1. Research background

1.1.1. Functional Surface of nature

Many of the creatures that exist in the nature have evolved over and over and have developed their own functional surface to survive at surrounding environments and showing amazing functional performance. (Fig. 1.1) The leaves of the plants have super-hydrophobicity to rolling off water droplets to achieve self-cleaning effects, and aquatic life protects the body from external substances such as oil by allowing water to be well contained around the body. In the case of water strider, can live on water using hydrophobic tiny hairy structure of its feet. The Namib beetles collect moisture from the atmosphere in the desert to earn the water to alive in extremely dry environment. And if we take a closer observation at these special functional surfaces, we can find that they have micro or nano-scale structures on their surfaces, and these structures play an important role to achieve the these functions. These creatures and micro/nano structures inspire us to better understand nature and get new ideas to solve the existing problems. Here, I studied fabrication of super-hydrophilicity surface and anti-oil/mineral-fouling capacities, via enhancing the surface roughness and wetting properties using plasma etching method. And, I suggest its application to the real environments.

Self cleaning

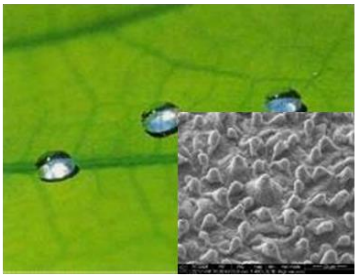

W. Barthlott, C. Neinhuis
Planta (1997) 202: 1-8

Self oil cleaning

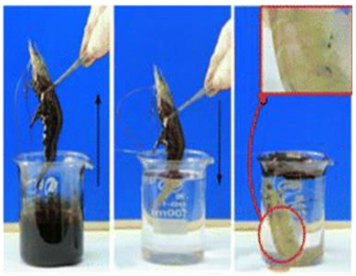

Shiyan Zhang et al.
ACS Appl. Mater. Interfaces (2013) 11971-11976

Water walking

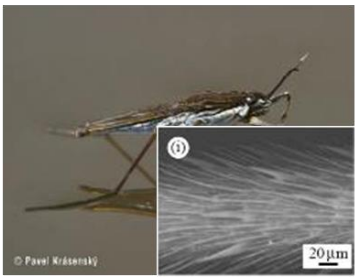

X. Gao & L. Jiang
Nature 2004 **432**, 36

Water harvesting

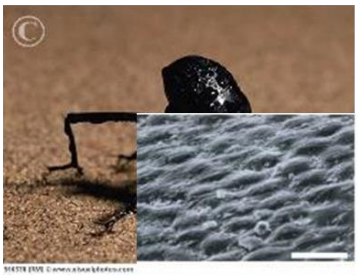

A.R. Parker *et al.*
Nature 2001 **414**, 33

Fig. 1.1 Functional surface of nature.

1.1.2. Research flow

The study focused on the Functional surface and proceeded with the following flow chart Fig. 1.2 The study started with observation of the phenomena in nature and it tried to applicate to the existing problems. Second, verification of the concerns and possible alternatives to solve them. Third, the studies had conducted found and verified examples of applications that can be used in real environments.

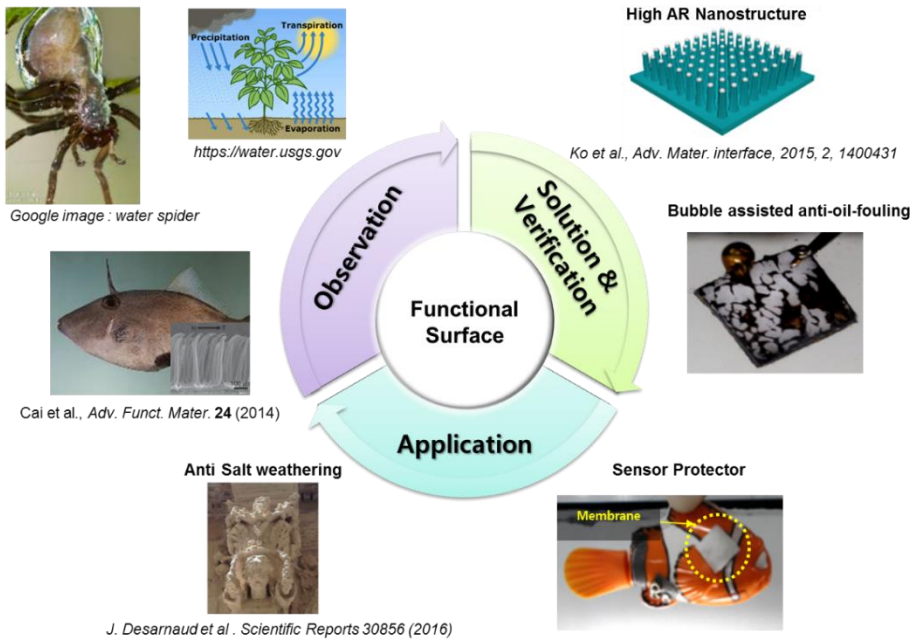

Fig. 1.2 Research flow

Chapter 2. Multi air-bubble enhanced oil rupture on nanostructured cellulose fabric for self-oil-cleaning under a dry state

2.1. Introduction

Oil is expected to remain an important source of energy as oil-related industries such as mining, transportation, and refining continue to grow despite the emergence of several alternative energy sources over the recent decades.[1] A greater demand for oil-spill management and efficient oil–water separation technologies is also expected because oil spill accidents occur in large sizes and in a wide range of locations. However, technologies dealing with oil spill responses still depend on conventional methods that have yet to overcome the limits of low-efficiency, high cost, and human-dependent control activities.[2-6]

To separate or remove spilled oil in water, sorbents, filters, or membranes having either hydrophobic/oleophilic or hydrophilic/underwater oleophobic surfaces have been intensively studied.[7] Among them, hydrophilic and underwater oleophobic materials have been heavily used recently because a hydrophilic surface is easily water-wetted, upon which the oil is repelled by water. Such materials have several advantages in various applications such as self-cleaning, anti-fogging, biocompatible materials, oil transportation, or oil-water separation.[8-11]

Additionally, oleophobicity and self-cleaning behavior can also be provided by superhydrophilic surfaces in the wetted state by water.[11-12] The significant disadvantage of existing superhydrophilic surfaces, however, is that they could be easily fouled by oil because of their high surface energy, thus losing their super-wetting characteristic.[13-16] It is also hard to re-wet by water and lose underwater oleophobicity due to the pre-absorbed oil that is hardly removed by water. Additionally, it was reported that once the textured surface is wetted by oil, it is very challenging to recover its super-hydrophilicity due to the strong capillary interactions between oil and the textured surfaces.[13, 16] Once fouled, especially on a structured surface with nanopores, the wetting transition from the Cassie-Baxter state to the Wenzel state is typically irreversible,[13] thus limiting their use in practical applications. Significant energy or work is necessary to overcome capillarity to push the infiltrated liquid out of the nanopores.[13, 17]

The critical technology of oil spill responds is the separation of oil from water. There are two main types of oil-water separation technology which are ‘oil removing type’ and ‘water removing type’. Fig. 2.1 shows the properties of each approach. Oil removing type is absorb the oil from the water such as oil absorbent and oil sponges. It is cheap and easy to purchase. However it causes a secondary environmental pollution that is managing the oil absorbed absorbent like bury or burn. Additionally, oil removing type filter easily clogged up with oil due to the intrinsic oil adhesion characteristics. On the other hands, water-removing type that

prevents oil fouling using water layer coating, and it removes water spontaneously by gravity.

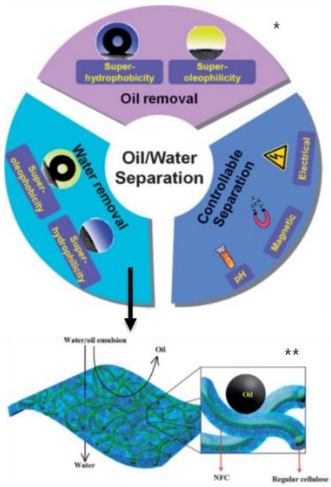

Type	Required Surface energy (SE)	Applications
Oil Removing (OR)	20~30mN/m < OR SE < 72 mN/m	Oil absorbent
Water Removing (WR)	WR SE < 20~30mN/m WR SE > 72 mN/m	Filter etc.

Type	Advantage	Disadvantage
Oil Removal	Easy to make	Easy to oil fouling
Water Removal	Protect from oil fouling Easy to oil-water separation by gravity	Hard to make Strict management

* Zhongxin Xue, et al, J. Mater. Chem. A, 2014, 2, 2445
** Kathleen Rohrbach, et al, *Chem. Commun.,* 2014, 50, 13296--13299

Fig. 2.1 Comparison of oil-water separation approaches

An unstable surface will decrease in terms of work efficiency during the oil–water separation process, and increase in cost, which requires a certain level of protection from oil contamination during use. Recent studies have presented anti-oil fouling hydrophilic surfaces under a dry state using a coating of zwitterionic polyelectrolyte.[16, 18-21] Surface coating using a polycrystalline TiO_2 thin film with ultra-violet irradiation or SiO_2-nano-particle added low-surface-energy polymers have also been reported to show an oleophobic nature in both air and underwater.[22-23] However, to use coating-based materials, such attempts require mechanical or chemical durability for many cycles during long-term use.[9]

2.1.1. Nature inspired solution for the existing problem

Diving bell spider (Water spider) is living underwater with air in its abdomen. Fig. 2.2 shows the structure of the abdomen, it covered with fine soft feathers, and each one of the hairs is made up of microscopic branches. In the schematic, the hydrophobic feathers which has air between them, it preventing water penetration. On the other hands,

We would inspired the air play a role in delaying the oil's penetration, and perhaps as a backpressure, and then push the oil out of the materials.

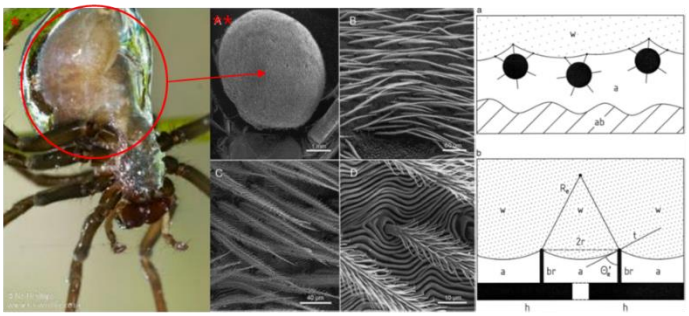

	Environment (Contact liquids)	Functional Requirement	Property	Realization
Diving Bell Spider	① Water contact	Water repel	Hydrophobicity	Hydrophobic & A Feather
		(using Trapped Air)	Aerophilicity	
Self-oil Cleaning Membrane at dry state	① Oil contact ② Water contact	Oil repel	Oleophobicity	**Oleophobic & Hydrophilic Material**
		(using Trapped Air)	Aerophilicity	
		Water affinity	Hydrophilicity	

* Google image
** Neumann and Woermann SpringerPlus 2013, 2:694

Fig. 2.2 Diving bell spider's hydrophobic feathers at abdomen which can trap air even in underwater.

2.1.2. Approach for the oil cleaning at dry environment

Herein, we present an easy-oil cleaning porous fabric made of hygroscopic, hydrophilic cellulose with nanostructures, which remains so even if oil-fouled before contact with water without any functional coating. Easy-oil cleaning by water was conducted by significantly increasing the retracting forces using nanostructures with a high aspect ratio (AR), the ratio of height over the width of the nanostructures, as well as through assistance from the air bubble, inducing oil mobility on the fibers. The buoyancy and backpressure induced in water recovered the wetting transition from the Wenzel (oil-fouled) state to the Cassie-Baxter (water cleaned) state reversibly. Selective oxygen plasma etching was used to provide a high AR for nanostructures and chemically hydrophilic hydroxyl groups, which strongly renders the hydrophilic fabric surfaces superhydrophilic, having the water contact angle near zero degrees in air. It was found that treated, oil-fouled fabric in a dry state is easily cleaned through immersion into water, as shown in Fig. 2.3 When a dried fabric is immersed into oil-covered water (Fig. 2.3a), the submerged fabric is initially fouled by oil at the oil–water interface, and the oil starts to recede on the fabric surface. During the oil receding process, air bubbles are observed at multiple sites of the fabric, lifting the oil residue (Fig. 2.3b). The air retained inside the porous fabric in a dry state are trapped by the oil covering during immersion into oily water, and as the covered oil is receded, air bubbles will also escape the porous fabric by pulling the oil droplets (Fig. 2.3c). The non-woven fabric has random roughness surface which hardly maintain the exact equal

experiment environment. To obtain the reliable data, we have conducted experiments more than three times. To investigate the anti-oil fouling characteristic even with oil fouling before water contact, we have conducted experiments for surface roughness enhancement, the air bubble effect, backpressure effect, cyclic test for durability, and practical application. The wetting property was controlled by two factors, chemical composition and roughness of the surface. [24] Oxygen plasma treatment enhanced the two factors simultaneously for hydrophilicity and underwater oleophobicity. The effect of oxygen plasma treatment was investigated in surfaces treated for up to 60 min and compared with the pristine (not treated) surface. The surface roughness was investigated by scanning electron microscopy (SEM) and Image J software. The oxygen plasma-treated surfaces were fouled by crude oil under the dry state and the oil receding behaviors were observed in the underwater state. The air bubbles induced by the oil-fouled fabric were observed and their effect on the oil receding behavior at underwater environment was evaluated. To evaluate the air bubble effect, we prepared pristine fabric and a 10 min oxygen plasma-treated surface that were also fouled by crude oil and immersed in water. Then, for each case, the induced air bubbles were removed using an oil absorbent. After the air bubble effect experiment, we also investigated the backpressure effect that was controlled by the thickness of the fabric. The prepared fabrics immersed in oil were covered by water. The fouled oil was observed to rupture and recede on the surface of the fabric assisted by air bubbles. We also conducted a cyclic immersion test for the duration of the underwater

oleophobicity. Finally, we demonstrated a practical application, namely, an oil-proofing sensor cover for underwater uncrewed vehicles.

We explored the effects of nanostructures and air bubbles on the oil cleaning of a cellulose fabric under a dry state. Furthermore, we conducted a cyclic immersion test, showing that the nanostructured cellulose surface, oil-fouled under a dry state, is continuously cleaned during cyclic immersion, whereas a pristine fabric without a nanostructure remains fouled on most of its surface. Finally, we applied an anti-oil fouling fabric as an underwater-sensor protective fabric to an oil-fouling operation in an oil-spilled environment.

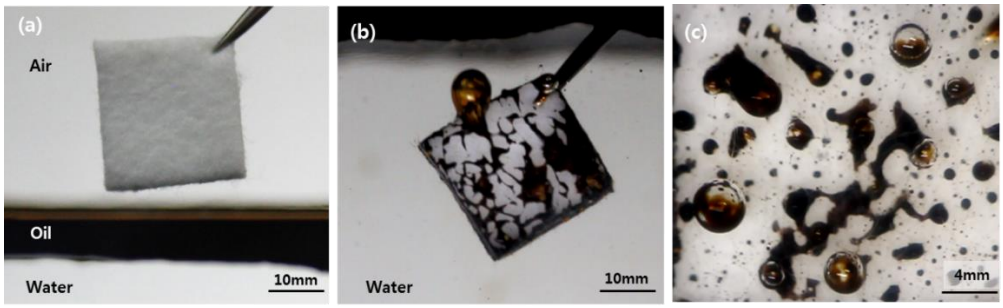

Fig. 2.3 (a) Dry rayon immersed in oil-covered water, (b, c) air bubbles retained in fabric pulling oil residue in water.

2.2. Result and Discussion

2.2.1. Oil cleaning on nanostructured hydrophilic fabric

Rayon fabrics, made from regenerated cellulose, were prepared under six different treatment conditions by choosing the oxygen plasma treatment duration, namely, no treatment (pristine), 1 min, 5min, 10min, 30 min and 60 min treatments, the results of which showed that the measured ARs of the nanostructures were 1.3, 8.0, 11.3, 37.2, and 55.9, respectively. A reduction in oil detachments was observed at 514, 311, 153, 124, to 135 s, respectively. Even though oil detachment was also observed on the surfaces treated by oxygen plasma for 1 (AR 1.3) and 5 min (AR 8.0), it was relatively slower than that in the other cases, where it occurred between 10 and 60 min. Therefore, the oil-repelling ability or speed was enhanced sufficiently after 10 min plasma treatment or an AR of 11. as shown in Fig. 2.7a. It was reported that the nanostructures were fabricated through the metal-incorporated dry ion etching process used in plasma treatment.[25] During the plasma treatment, metal particles are sputtered from the cathode plate and then co-deposited onto the rayon surface.(Fig. 2.4) These metal particles act as an etching mask upon which the polymer surface shows a low etching rate for oxygen plasma. However, the regions where these metal particles are not deposited have a high etching rate depending on the plasma treatment duration, and thus are easily etched, eventually forming a high AR nanostructure.[25]

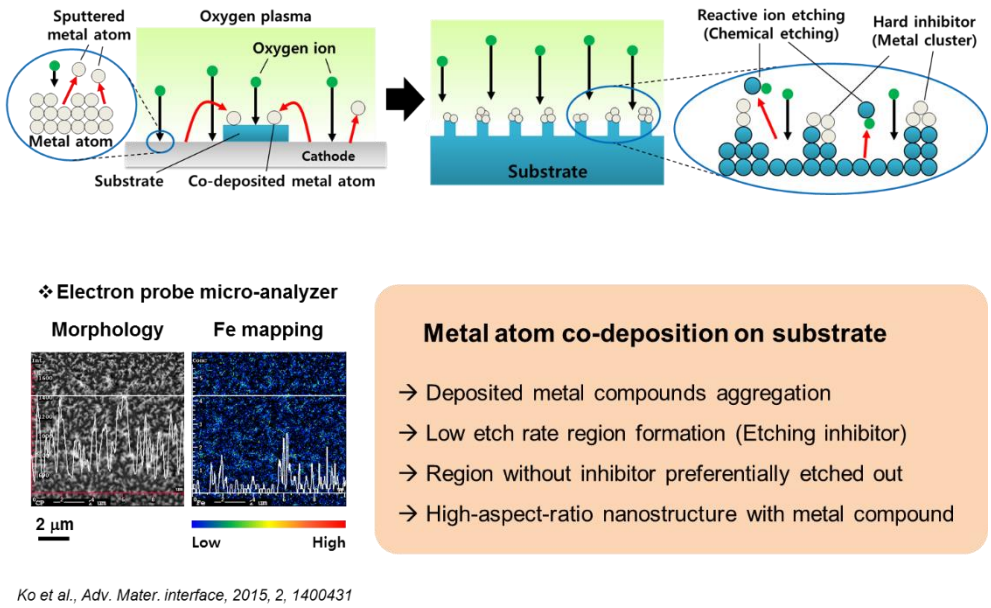

Fig. 2.4 Fabrication of high-aspect-ratio nanostructures using O2 plasma treatment

The oil contact angle and detachment time were measured in water (Fig. 2.5) on the three different fabric surfaces. The pristine rayon fabric fouled by oil droplets in a dry state was immersed in water, and the oil residue started to recede and increased the oil contact angle after 110 s, fully detaching with an oil contact angle of approximately 110° after 40 mins. It was observed that the pre-wet rayon fabric has a strong oil repellent nature in comparison to the dry fabric, as shown in Fig. 2.5, owing to the presence of a water film between the oil and rayon.

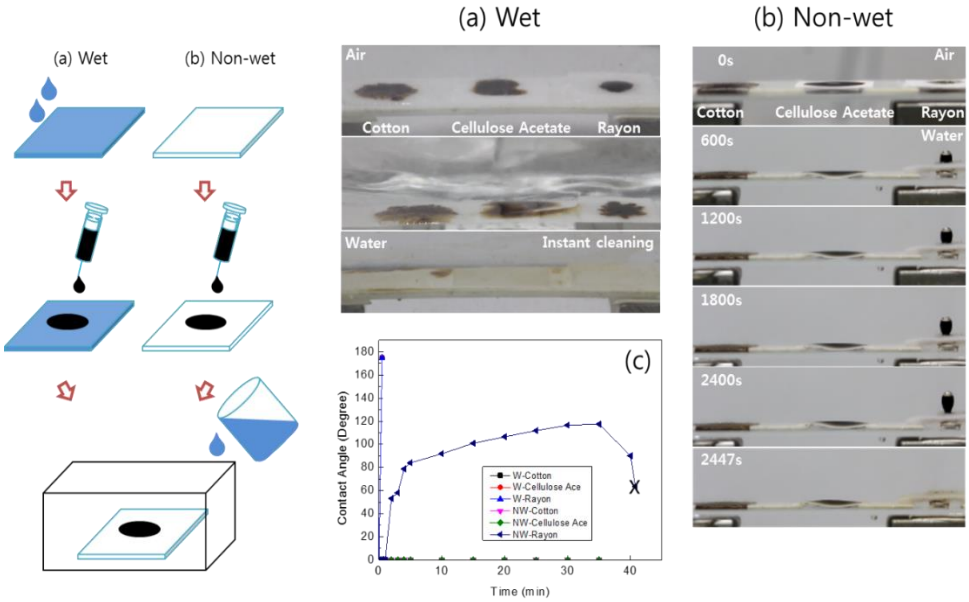

Fig. 2.5 Oil cleaning of hydrophilic fabrics, (a) crude oil on the wet fabrics were instantly cleaned by water, (b) crude oil on the non-wet fabrics was not easily removed, only oil residue on rayon was showed to detach from the surface, (c) oil contact angle changed with time.

2.2.2. Oil cleaning on nanostructured hydrophilic fabrics

The pristine rayon fabrics were prepared for oil cleaning experiment in both wet and dry states as shown in Fig. 2.6. First, crude oil was dropped on the water-wet fabric (left side). As soon as immersed in water, the oil on the wet fabric was immediately detached. Since rayon fabric was pre-wet by water of the rayon fibers, oil would not be easily fouled on the wet fabric.[7] On the other hand, the oil was dropped on the dried rayon fabric remained fouled strongly underwater as shown in the sequential images of Fig. 2.6 (right side). Oil residue on rayon fabric was receded to form a large oil droplet surrounded by smaller droplets. During this process, it was clearly found that the oil droplet has the air bubbles on each oil drop regardless of its size, which pulled the oil droplet away from the fabric after 2,400 sec. As compared in Table 1, the water-wet rayon has strong oil resistance since the water gain rate of rayon is higher than cotton or cellulose acetate.[15] The higher fraction of amorphous structure over crystalline structure in rayon fibers. Previous studies showed that the moisture regain of cellulose is linearly related to the fraction of amorphous.[16-19] Ciolacu et al also suggested that water sorption occurred almost totally in the amorphous domain of cellulose.[20] Mann and Marrinans showed that the readily accessible part can be approximately identified with the amorphous regions, while the slowly accessible component is a part of the crystalline fraction of the cellulose.[21] It means that the rayon has a higher wicking rate, which can provide a bigger retracting force to the fouled oil as absorbed water.

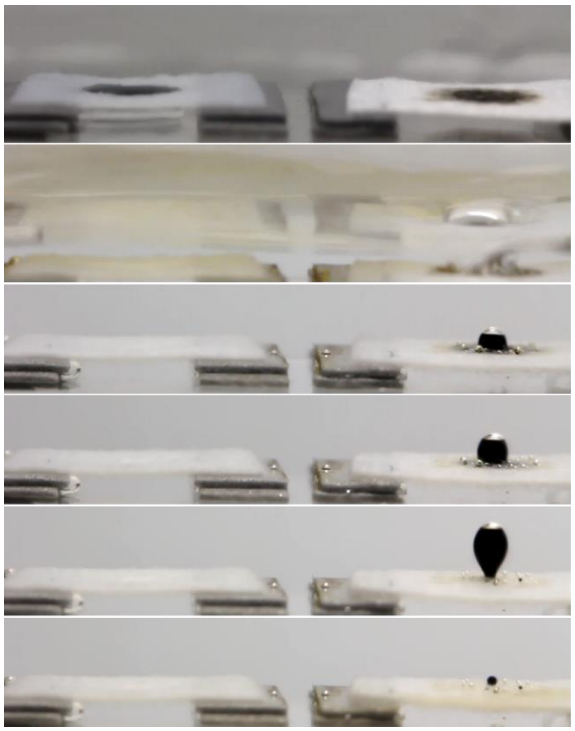

Fig. 2.6 The oil cleaning sequence on the oil fouling on the wet (left) and dry (right) state fabrics in water. Scale bar is 2mm.

Table. 1 Properties of cellulose based hydrophilic fabrics

		Cotton	Rayon	Structure of Cotton & Rayon
Water gain rate (fiber mass)	in Air	8%	14%	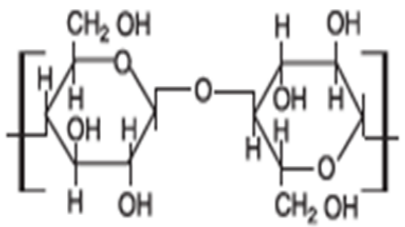
	in Water	30%	70%	
Oil sorption rate (g)		33g/g	19g/g	
Crystalline/Amorphous		over 60% / 40%	About 30% / 70%	
Molecular weight		A	A/5	

Gupta, B. S., Bio textiles for medical applications. (2013)

The rayon fabrics with 3 different treatment conditions were prepared by choosing oxygen plasma treatment duration of pristine (no treatment), 10 and 30 min, showing that the AR of nanostructures on each fabric were varied from 11 to 37 in Fig. 2.7a. It was reported that the nanostructures were fabricated through metal-incorporated dry ion etching process of plasma treatment. During the plasma treatment, metal particles would be sputtered from the cathode plate and then co-deposited on the rayon surface. These metal particles act as an etching mask on which the polymer surface show a low etch rate for oxygen plasma. However, the regions where these metal particles are not deposited has a high etching rate depending on the plasma treatment duration, so that they are easily etched and eventually a high aspect ratio nanostructure is formed.[14] The oil contact angle and detachment time were measured in water (Figs. 9b and 9c) on 3 different fabric surfaces. The pristine rayon fabric fouled by oil droplet in dry state was immersed in water and the oil residue started to recede and increase its oil contact angle after 110 sec and fully detached with oil contact angle around 110o after 40 mins. However, the nanostructured rayon (30min duration, AR~37) fabric fouled by oil droplet showed the increases in oil contact angle upto 157o after 100 secs and was fully detached within 2 mins.(See Fig. 2.7c) Furthermore, in all cases of pristine and nanostructured surfaces, air bubbles formed on top of the oil droplets were observed to pull oil residues off from the fabrics. It can be presumed that the air bubbles would contribute oil receding and detachment by adding the addition

forces for the oil drop upward against the interface adhesion strength between oil and the fabric surface.

In contrast, a nanostructured rayon fabric fouled by oil droplets in a dry state (30 min duration, AR of ~37) showed a relatively faster oil detachment by increasing the oil contact angle up to 157° after 100 s, reaching full detachment at 2 min (see Fig. 2.7c). It was found that in all cases of pristine and nanostructured surfaces, air bubbles that had formed on top of the oil droplets were observed to pull the oil residue off of the fabric. It can be presumed that the air bubbles contributed to the oil receding and detachment by adding additional upward forces to the oil drops against the interface adhesion strength between the oil and fabric surface.

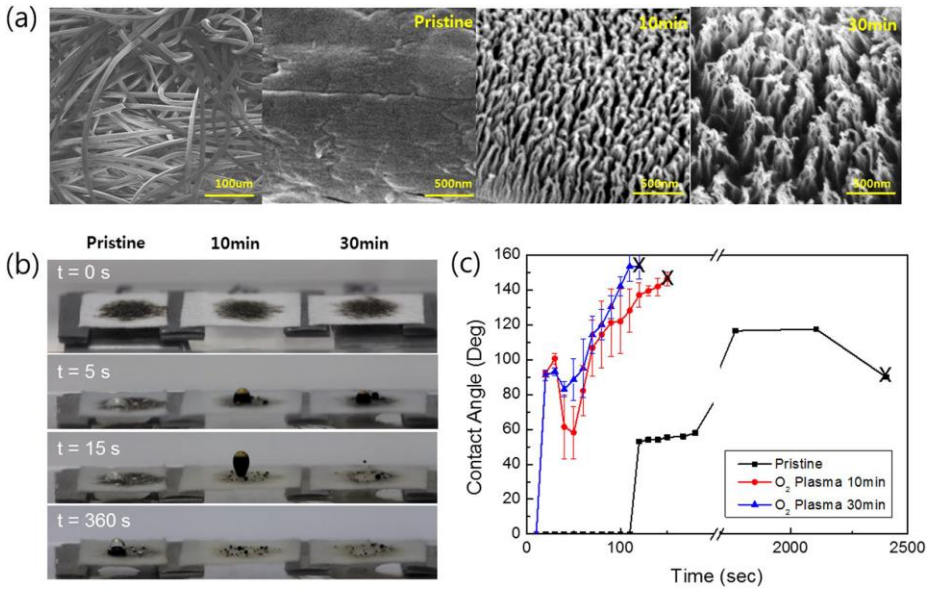

Fig. 2.7 (a) SEM images of the surface morphology for surfaces of pristine nonwoven rayon fabric and nanostructured surface with O2 plasma treatment of 10 and 30 min. (b) Oil releasing behavior on the pristine and nanostructured surface in water and (c) oil contacting angle traced in water over time.

2.2.3. Nanostructure-enhanced oil detachment with air bubbles and backpressure

To explore the role of air bubbles on the oil detachment, experiments with and without air bubble on top of the oil drop was conducted, as shown in Fig. 2.8. First, the dry rayon fabric was fouled by 10 μl of crude oil in an air environment, and placed into water to compare the underwater receding behavior of the triple contact line of oil/water/solid for the different surface conditions. The oil detachment force can be described by the following equation as schematically shown in Fig. 2.8e:

$$F_{detach} = F_B^{oil} + F_B^{air} + F_{cap}, \qquad (1)$$

where F_B^{oil} is the oil buoyancy (=$(\rho_{water}-\rho_{oil})gV_{oil}$), F_B^{air} is the air buoyancy (= $(\rho_{water}-\rho_{air})gV_{air}$), ρ is the fluid density, g is the gravitational acceleration, and V is the fluid volume. F_{cap} is the capillary force acting at the contact line and is estimated as

$$F_{cap} = 2\pi R_c \gamma_{ow}(\cos\theta - \cos\theta_s), \qquad (2)$$

where γ_{ow} is the interfacial tension between oil and water, and θ and θ_s are dynamic and static contact angles of an underwater oil droplet on the fabric, respectively. Note that F_{cap} is positive when $\theta < \theta_s$, which acts to detach the oil, while it is negative when $\theta > \theta_s$, which plays the role of capillary adhesion that resists oil detachment. For the pristine fabric, the air bubbles were observed to have a significant effect, especially in a later stage of the oil detachment, by pulling the oil up through the air buoyancy of $F_B^{air} \approx 36$ μN along with the receding capillary force. e.g. $F_{cap} \approx 15$ μN at 2400 s, where a θ_s of 129° is used on the pristine fabric

(Fig. 2.8a). This is contrary to the case without air bubbles in which F_B^{air} is nearly zero because the air bubble is removed when it is pricked with a hydrophobic absorbent (Fig. 2.8b).[26] These air bubbles arise from the micro-pores of the fabric owing to ~~air~~ buoyancy after the oil had covered these pores. Subsequently, as shown in Fig. 2.8a, the oil droplets are elongated vertically, and meanwhile, the contact line recedes at a low speed. This temporal behavior is plotted in Fig. 2.8g using the ratio of the oil contact radius (R_c) to the initial contact radius ($R_{c\text{-}ini}$). When the contact radius decreases to a specific value ($R_c/R_{c\text{-}ini} \approx 0.4$), the oil column near the solid surface is rapidly pinched off after 2,447 s owing to vigorous capillary pumping out of the necked location.[27-28] The oil remaining below the pinch-off location does not recede further because it lacks air bubbles to be drive the receding oil. In other words, F_B^{oil} (≈ 0.4 μN) and F_{cap} (≈ 35 μN) of the remaining oil are not enough to further cause oil detachment by overcoming the viscous adhesion (F_{vis}) of the oil fouling between the fibers. In contrast, an oil droplet with no air bubble (Fig. 2.8b) shows extremely slow retraction of the contact line on pristine rayon in water, which indicates the effect of air buoyancy on the receding contact line. The oil then recedes at a low speed for nearly 4 h ($\approx$ 13,920 s) and stops, further receding when it reaches the static contact angle because the oil buoyancy (≈ 8 μN) is insufficient to overcome the capillary adhesion as well as the viscous adhesion,

Nanostructured cellulose fabric (Fig. 2.8c–d) presents an essential difference in the oil receding performance in comparison to pristine fabric. Regardless of

whether air bubbles are present, the oil droplets were removed from the solid surface within ≈ 1 min. The static contact angle does not remain stable. Instead, it diverges as $\theta \rightarrow 180°$ on the nanostructured cellulose fabric. Thus, F_{cap} is always positive on the nanostructured fabric and is supposed to detach the oil with a stronger force than that acting on the pristine fabric. Additionally, the relatively minor difference caused by the air bubbles is that the oil droplets with air bubbles initially recede faster than those without air bubbles owing to additional air buoyancy, and then pinch off quite quickly at 43 s, with a residual amount left on the solid surface (Fig. 2.8c). However, unlike the pristine case, the residual oil further recedes and detaches from the solid surface for the nanostructured fabric. The remarkable performance of the nanostructure over the air buoyancy originates from the partial contact of oil with a hydrophilic nanostructure, which is in contrast with the full contact on the pristine fiber, as schematically compared in Fig. 2.8f. This partial contact contributes to boosting the receding contact line by enhancing F_{cap} from diverging θ_s as well as alleviating the viscous adhesion (F_{vis}) of oil fouling between the fibers, which can be quantified by measuring the contact angle hysteresis (CAH) [29-33]

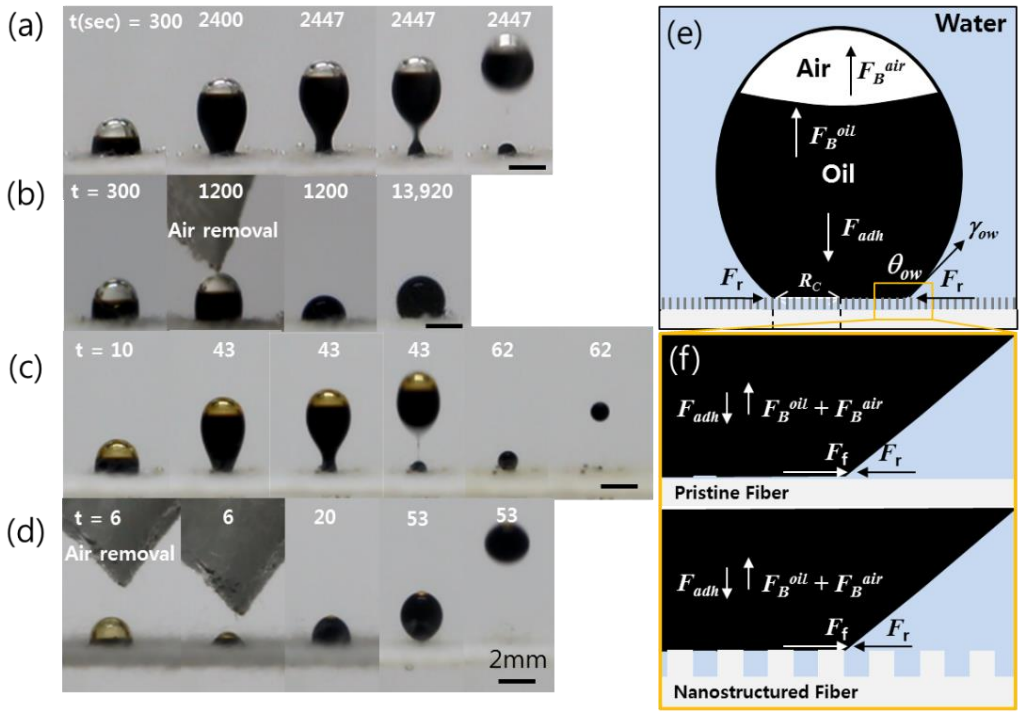
(a)
t(sec) = 300
2400
2447
2447
2447
(b)
t = 300
1200
Air removal
1200
13,920
(c)
t = 10
43
43
43
62
62
(d)
t = 6
Air removal
6
20
53
53
2mm
(e)
Water
Air
F_B^{air}
F_B^{oil}
Oil
F_{adh}
γ_{ow}
θ_{ow}
F_r
R_C
F_r
(f)
F_{adh}
$F_B^{oil} + F_B^{air}$
F_f
F_r
Pristine Fiber
F_{adh}
$F_B^{oil} + F_B^{air}$
F_f
F_r
Nanostructured Fiber

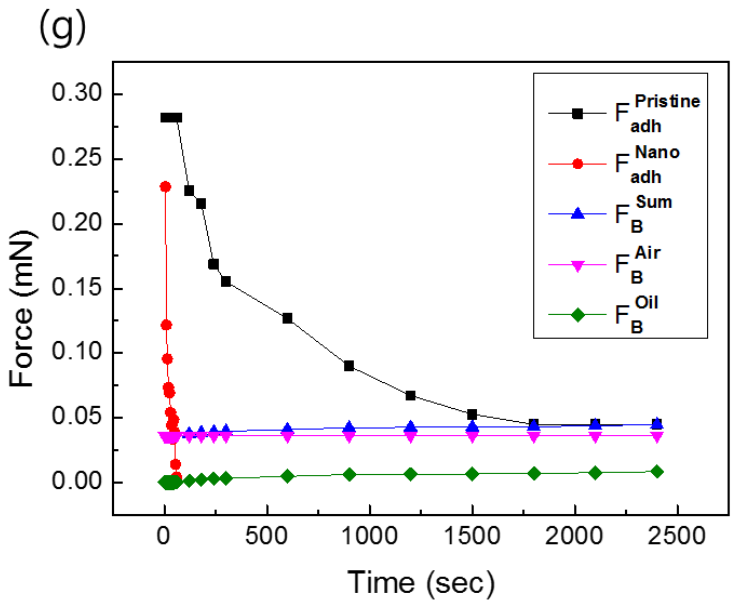
(g)
Force (mN)
0.30
0.25
0.20
0.15
0.10
0.05
0.00
0
500
1000
1500
2000
2500
Time (sec)
$F_{adh}^{Pristine}$
F_{adh}^{Nano}
F_B^{Sum}
F_B^{Air}
F_B^{Oil}

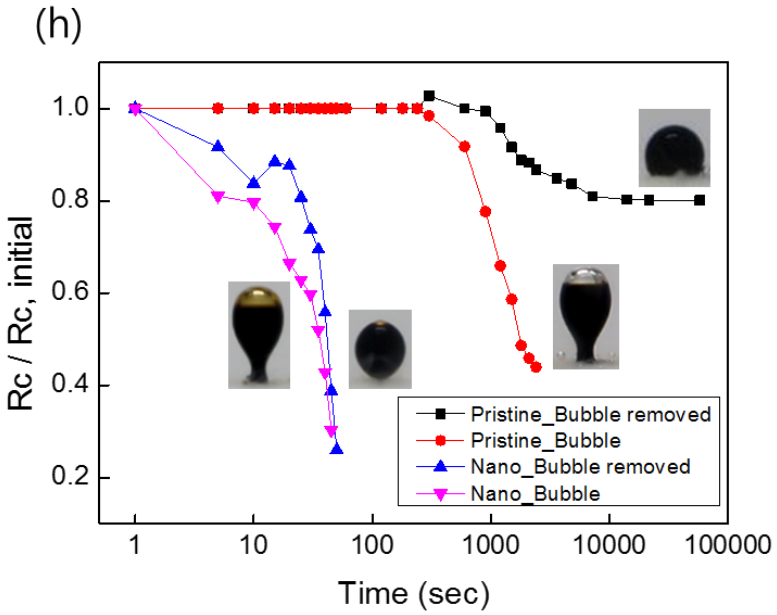

Fig. 2.8 Sequential images of oil receding on rayon surface with/without bubbles and nanostructure in water over time. Oil droplet on the pristine rayon surface (a) with and (b) without air bubbles, and a nanostructured surface (c) with and (d) without air bubbles. Oil receding model with forces acting near oil droplet on nanostructured surface in water. (e) and (f) Schematic of force balance of oil and air bubbles. (g) Vertical Force balance as the oil volume increases on the pristine fabric. (h) Ratio of oil contact radius ($\boldsymbol{R_c}$) to the original oil contact radius ($\boldsymbol{R_{c-ini}}$) with/without air bubbles and nanostructure fabric.

The extreme difference in CAH between the pristine and nanostructured surfaces is demonstrated, which shows that an oil droplet is firmly stuck to pristine rayon even up to a sliding angle of ≈ 90° in an underwater environment. In contrast, the oil on nanostructured rayon easily rolls off at a sliding angle of ≈20°, which contrasts the superior property of the low CAH of nanostructured rayon. (Fig. 2.9) This low CAH is caused by partial contact between oil and a solid fiber with a nanostructure, which is referred to as the Cassie–Baxter state. [30] The Cassie–Baxter state on the nanostructure also implies that the air-pocket is capable of sticking between the nano-pillars of the rayon even when fouled by oil in a dry environment. Later, when put into water, this trapped air further pushes off the oil drop on top of the nanostructure as the water wicks through the fabric with the pushing air. This air beneath the oil droplet is known to act as a backpressure with improved liquid mobility by inducing a de-pinning of the oil [34-36], as schematically shown in Fig. 2.10d. For the nanostructured rayon fiber to have a high AR, the air backpressure acts at numerous locations even on a single fiber, which is thought to essentially boost the de-pinning by significantly reducing the de-pinning distance down to the nano-scale pitch between adjacent nano-pillars.

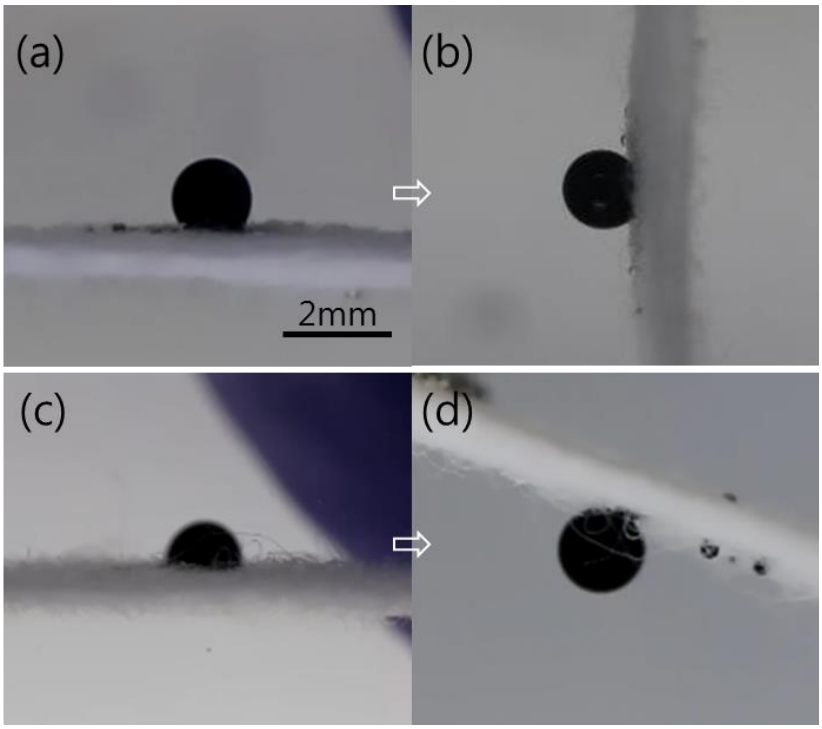

Fig. 2.9 Underwater CAH measurements on the pristine and nanostructured rayon. (a) Air bubble removed oil on the pristine rayon. (b) The sample (a) was tilted 90º, but the CAH cannot measured due to the oil was sticking. (c) Air bubble removed oil on the nanostructured rayon. (d) The sample (c) was rotated 180º rapidly to prevent the oil detachment and the CAH hard to measured due to the oil was rolling at around 20º

Owing to this low CAH, the oil can be driven to recede by the so-called uncompensated Young's force (= $2\pi Rc\ \gamma ow(\cos\theta - \cos\theta r)$) when $\theta < \theta r$,[27] where θr is the receding contact angle. The maximum force is ≈ 68−271 μN at $\theta = 0°$, which should overwhelm the oil buoyancy. Please note that the receding capillary force is zero on the pristine fabric as $\theta r \rightarrow 0°$. The Cassie–Baxter state on the nanostructure also implies that the air-pocket is capable of sticking between the nano-pillars of the rayon even when fouled by oil in a dry environment. Later, when put into water, this trapped air further pushes off the oil drop on top of the nanostructure as the water wicks through the fabric with the pushing air. This air beneath the oil droplet is known to act as a backpressure with improved liquid mobility by inducing a de-pinning of the oil [30-32], as schematically shown in Fig. 2.10d.

2.2.4. Air-bubble induced oil cleaning

Here, to further explore the air-bubble effect on the oil detachment, we varied the thickness of the fabric, which equivalently changed the total amount of air trapped in the microporous fiber network. The thicknesses of the prepared fabrics were 1.5, 2.6, and 5.2 mm, as shown in Fig. 2.10a. It can be seen that the oil immediately fouled all surfaces in air, and then receded with a different detachment behavior over time underwater. The oil receding time is shorter for the thicker sample (5.2 mm) in comparison with the thinner sample (1.5 mm). The thickness effect is more dramatic in comparison with the samples after 10 min of O_2 plasma treatment owing to the presence of the nanostructure. Furthermore, the effects of the bubbles can be clearly identified during the early stage. After 1 s of oily water immersion, most of the area for the thin fabric without a nanostructure is fouled by oil, and a larger area was cleaned by bubbles until 90 s. With an increased thickness of the samples, the fouling rate of oil residue shortens and is significantly enhanced with the nanostructures. The oil fouling rate, which is defined as the oil covered area over the total surface area of each sample over time, was traced in water. As indicated in Fig. 2.10b, the oil fouling ratio measured for a thicker sample has a steeper slope than that for a thin sample. Furthermore, the nanostructured samples are further enhanced in terms of the oil fouling rate for both thicknesses.

(a)

Sample	Thick-ness (mm)	Time (sec) 0	1	3	5	30	90
Pristine	1.5	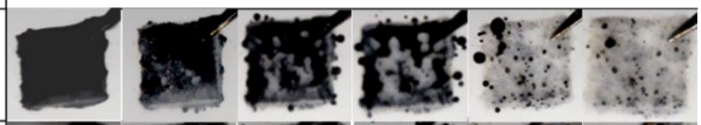					
	2.6	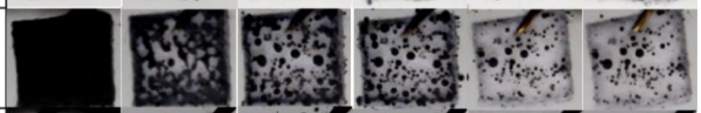					
	5.2						
Nano-structured With 10min O_2 Plasma	1.5	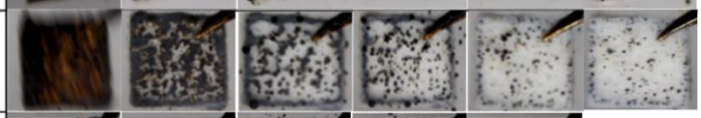					
	2.6	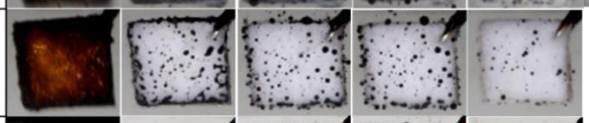					
	5.2	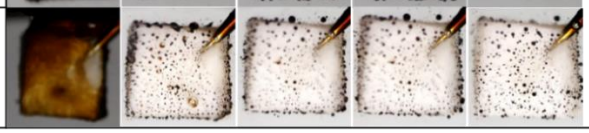					

(b)

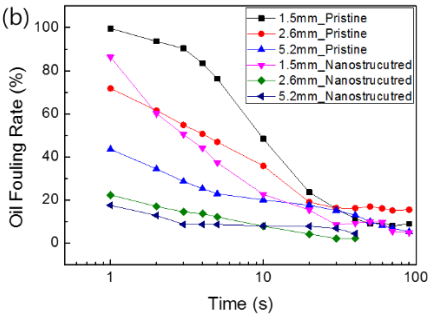

(c)

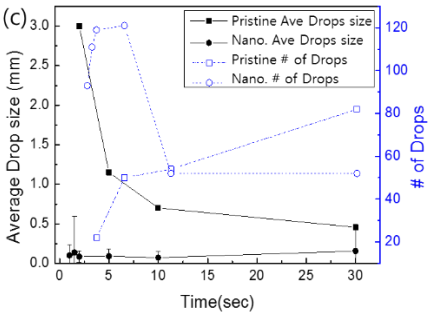

(d)

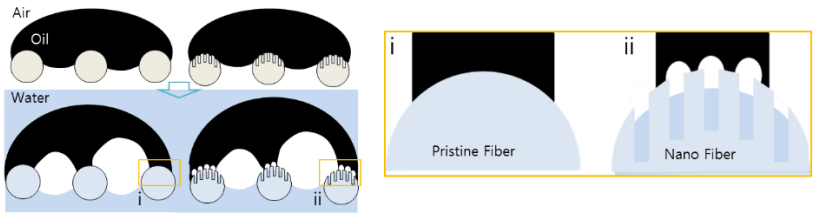

Fig. 2.10 (a) Optical sequential images for oil cleaning on fabrics with and without nanostructures for three different thicknesses. (b) Oil fouling ratio for thicker sample having a steeper slope than that for the thin sample. Furthermore, the nanostructured samples are further enhanced in terms of the oil fouling rate for both thicknesses. (c) Pristine surface without nanostructures and relatively larger oil residues. In contrast, in the case of the nanostructured fabric, smaller oil residues were observed. (d) Schematic of air-bubble induced process on pristine and nanostructured fabrics.

However, non-woven structures of the fabric trapped some oil droplets, despite the oil receding completely and detaching from the single nanostructured fibers. Fig. 2.11 shows the oil trapped by adjacent fibers. It has completely receded with an almost spherical shape. In the case of a nanostructured fabric, it was observed that the size of the oil residue is smaller than that of the pristine fabric shown in Fig. 2.10c. In the case of the pristine surface without a nanostructure, the relatively larger oil residue of approximately 2–3 mm in radius was mainly formed at the beginning of the water immersion test, and the small sized residues increased over time. In contrast, in the case of the nanostructured fabric, a smaller oil residue of approximately 0.1–0.2 mm was observed over multiple sites. It was reported that the oil droplets are small on the nanostructure surface because the energy barrier for rupturing is low owing to the viscous adhesion force, F_{vis}, between the oil and solid, which is significantly low from the lower solid fraction. [37-39]

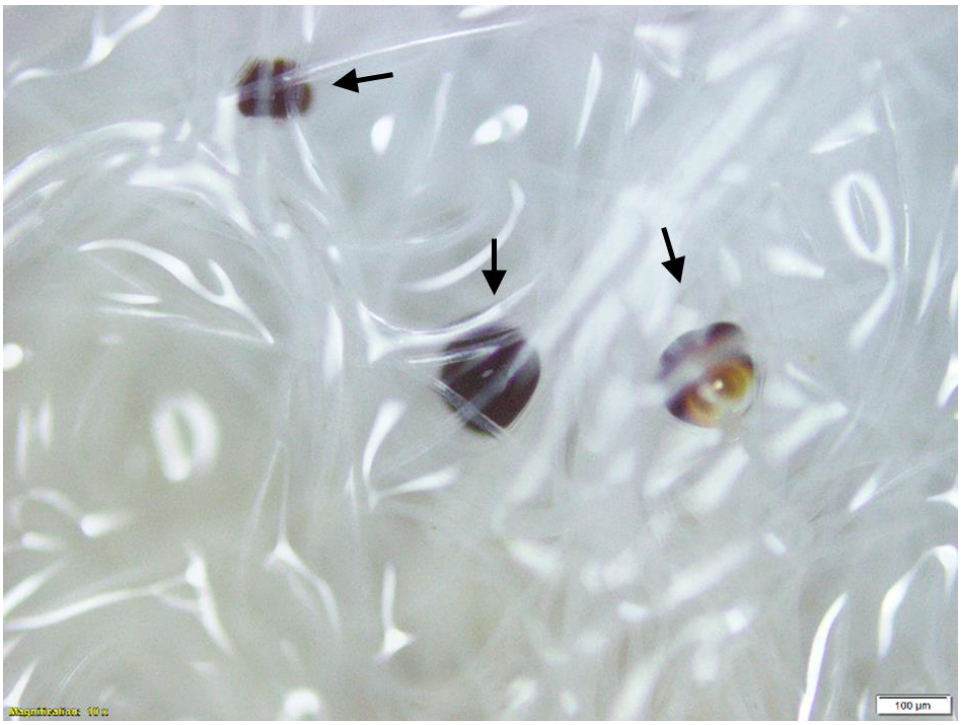

Fig. 2.11 Optical microscopy image of oil trapped in rayon non-woven fabrics. The oil receded entirely and exhibited an almost spherical shape. However, it could not escape from the fabrics because adjacent or crossed fibers blocked the release of the trapped oil (arrowed).

2.2.5. Cyclic test for self-oil-cleaning

We further explored the oil detachment behavior on the samples by applying a cyclic immersion test into oily water. A dry rayon sample of 2.6 mm in thickness was immersed in oil covered water, and ten cycles of a pull out/immersion experiment were applied, as shown in Fig. 2.12a. First, for immersion into oily water (see the representative image ① in Fig. 2.12b), the dried rayon was immediately fouled (②), and remained for 40 s underwater reaching a steady state to allow the oil to recede (③) from the nanostructured or pristine fabric. The sample was taken out of the water tank and immersed into water again (④). Continuing with this cycle, the oil fouling ratio of the pristine fabric decreased from 73% to 47% (⑤ in Fig. 2.12c), and then remained at approximately 40% at the tenth cycle (⑥). However, the oil fouling ratio of the nanostructured fabric was measured as 6.5% for the first cycle (⑦), and then maintained an oil residue of around 5% at the tenth cycle (⑧). Representative images of the oil fouling fabric surface in each step (Fig. 2.12c) were taken, and are shown in Fig. 2.12d.

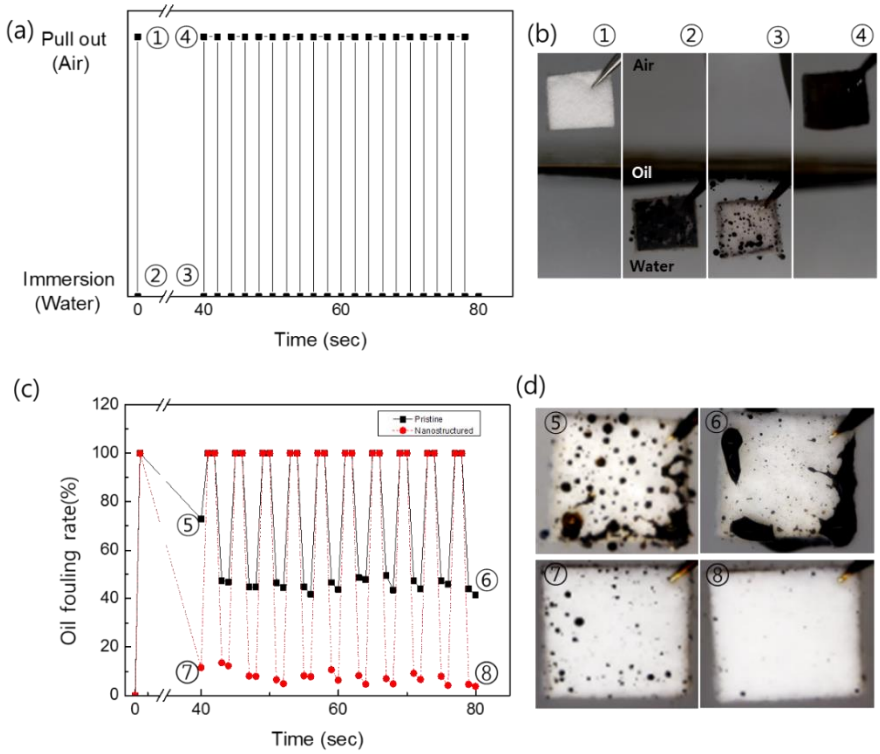

Fig. 2.12 (a) Cyclic immersion test condition in oily water for ten cycles and (b) representative images of rayon fabric at each position in (a) air and water. (c) Oil fouling rate measured on the pristine (black squire) and nanostructured (red circle) fabric surfaces and (d) its representative images. All samples in (b) and (d) are 10 mm × 10 mm in size with a thickness of 2.6 mm.

2.2.6. Oil-proofing sensor cover for robot fish

Finally, we applied the fabric to a protective material for the sensing system of a robot fish swimming in oily water. Underwater sensors are used for many different applications, which require several special functions such as anti-bio or mineral fouling. In addition, the sensors working under an oily environment should be equipped with an anti-oil fouling or oil-proofing surface. We covered the eyes of the robot fish with a nanostructured fabric. The robot fish was designed to swim by moving its tail fin when immersed in water. The motor for the moving tail fin is operated by detecting the electronic conductivity through the two eyes in a conductive water environment. If one or both eyes are blocked by a non-conductive substance such as oil, the electronic signal is cut off and the robot fish can no longer move. When immersed in fresh water, the robot fish swims freely, as shown in Fig. 2.13a. When the robot fish was placed in oily water, it did not move at all owing to the non-conductive oil completely covering both of the sensors, as shown in Fig. 2.13b. However, when the robot fish with the nanostructured fabric was placed into oil-covered water, the eyes were oil-proof but water was allowed to flow through the membrane, allowing the fish to move freely underneath the oily water (Fig. 2.13c).

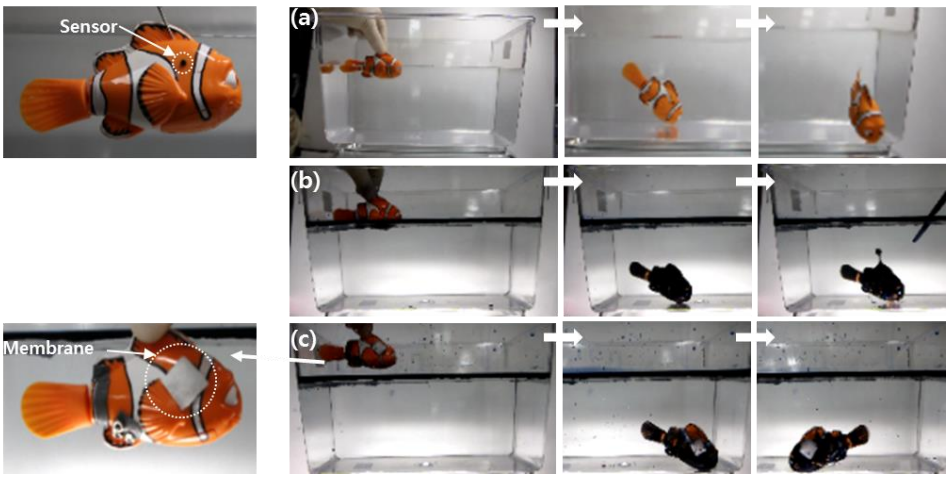

Fig. 2.13 A demonstration of oil-proof or oil-cleaning fabric used as a protective cover on conductive sensors on a robot toy swimming in water. A robot swimming (a) in fresh water without fabric, (b) in oily water without fabric, and (c) in oily water with fabric. The length of the robot toy is approximately 70 mm.

2.3. Conclusion

In conclusion, a quick oil-cleaning surface even under a dry state of oil fouling was suggested for use in cellulose fabric with a high AR nanostructure. The anti-oil fouling under a dry state was realized through two main features: a low solid fraction with high AR nanostructures significantly increasing the retracting forces and number of air bubbles trapped between the fibers and nanostructure under a dry state, thereby increasing buoyancy, and multiple backpressures enhancing the oil layer rupture. The nanostructured fabric was continuously cleaned during cyclic immersion into oily water, whereas the pristine fabric remained fouled owing to the slow oil cleaning of the initial oil fouling. It can be understood that anti-fouling under a dry state can be induced by the air bubbles formed in multiple locations, whereas the anti-fouling under a wet state would be induced by the water coating on the nanostructured surface. Further, we demonstrated the application of oil-proofing fabric for protecting the underwater conductive sensors on a robot fish from oil fouling, while allowing the conductive water to penetrate the sensors. Along with various applications for oil–water separation membranes or cleaning devices, such an oil-cleaning fabric with a nanostructure can be applied to the oil-proof surfaces for several oil-field devices or ships exploring or traveling in oil-contaminated areas.

2.4. Methods

Non-woven rayon fabric, which was hydrophilic and with underwater oleophobicity, were purchased from a commercial company (catalog # SPL80(FC)V Nam Yang Non-Woven Fabric Co., South Korea). The non-woven type fabric was prepared at a size of 2.5 cm × 2.5 cm and with a density of 158.5 kg/m3. Oxygen plasma etching was utilized to form the nanostructures on the rayon fibers using a custom-built plasma etching device having the plasma power and substrate bias voltage set at 230 W and 400 V, respectively.[14] With an oxygen gas flow rate of 100 sccm, the plasma treatment duration applied was 10 and 30 min, resulting in various ARs, namely, 11.4, and 37.4, respectively.

The surface morphology was explored using a scanning electron microscope (SEM, Inspect-F, FEI, USA). A 6-nm thick Pt film was covered onto the fabric to provide better conductivity and prevent the generation of an electron charge on the polymeric fabric. The SEM electron accelerating voltage was 7 kV. The contact angle (CA) of oil was measured using underwater conditions for a light crude oil of 0.87 g/ml in density (Hyundai Oil Bank Co., South Korea) and droplets with a volume of 10.0 ± 0.5 μl. A water immersion test was conducted on various fabrics and recorded with a digital camera with a resolution of 15 megapixels (Canon EOS 60D).

2.5. References

[1] Oil Tanker Spill Statistics 2017. *ITOPF*, **16**, (2018).

[2] Kim, D. H. et al. UV-responsive nano-sponge for oil absorption and desorption. *Sci Rep*, **5**, 12908 (2015).

[3] Fingas, M. *The basics of oil spill cleanup*. CRC press (2012).

[4] Choi, H. M. & Cloud, R. M., Natural sorbents in oil spill cleanup. *Environ. Sci. Technol.*, **26**(4), 772-776, (1992).

[5] Lin, J., Shang, Y., Ding, B., Yang, J., Yu, J. & Al-Deyab, S. S. Nanoporous polystyrene fibers for oil spill cleanup. *Mar Pollut Bull*, **64**(2), 347-52, (2012).

[6] Xue, Z., Cao, Y., Liu, N., Feng, L. & Jiang, L. Special wettable materials for oil/water separation. *J. Mater. Chem. A*, **2**(8), 2445-2460, (2014).

[7] Xue, Z. et al. A novel superhydrophilic and underwater superoleophobic hydrogel-coated mesh for oil/water separation. *Adv. Mater.*, **23**(37), 4270-4273, (2011).

[8] Liu, M., Wang, S. & Jiang, L. Nature-inspired superwettability systems. *Nat. Rev. Mater.*, **2**(7), 17036, (2017).

[9] Yong, J., Chen, F., Yang, Q., Huo, J. & Hou, X. Superoleophobic surfaces. *Chem Soc Rev*, **46**(14), 4168-4217, (2017).

[10] Jiang, T., Guo, Z. & Liu, W. Biomimetic superoleophobic surfaces: Focusing on their fabrication and applications. *J. Mater. Chem. A*, **3**(5), 1811-1827, (2015).

[11] Kobayashi, M., Terayama, Y., Yamaguchi, H., Terada, M., Murakami, D., Ishihara, K. & Takahara, A. Wettability and antifouling behavior on the surfaces of superhydrophilic polymer brushes. Langmuir, 28, 7212-22, (2012).

[12] Marmur, A. Underwater superhydrophobicity: theoretical feasibility. Langmuir, 22,

1400-1402, (2006).

[13]Liao, Z., Wu, G., Lee, D. & Yang, S. Ultrastable underwater anti-oil fouling coatings from spray assemblies of polyelectrolyte grafted silica nanochains. ACS Appl. Mater. Interfaces, 11, 13642-13651, (2019).

[14]Drelich, J., Chibowski, E., Meng, D. D. & Terpilowski, K. Hydrophilic and superhydrophilic surfaces and materials. Soft Matter, 7, 9804-9828,(2011).

[15]Occhiello, E., Morra, M., Morini, G., Garbassi, F. & Humphrey, P. Oxygen-plasma-treated polypropylene interfaces with air, water, and epoxy resins: Part I. Air and water. J. Appl. Polym. Sci. 42, 551-559, (1991).

[16]He, K.; Duan, H.; Chen, G. Y.; Liu, X.; Yang, W.; Wang, D., Cleaning of Oil Fouling with Water Enabled by Zwitterionic Polyelectrolyte Coatings: Overcoming the Imperative Challenge of Oil-Water Separation Membranes. *ACS Nano*, ***9*** (9), 9188-98, (2015).

[17]Krupenkin, T. N., Taylor, J. A., Schneider, T. M. & Yang, S. From rolling ball to complete wetting: the dynamic tuning of liquids on nanostructured surfaces. Langmuir, 20, 3824-3827, (2004).

[18]Shi, C., Yan, B., Xie, L., Zhang, L., Wang, J., Takahara, A. & Zeng, H. Long-range hydrophilic attraction between water and polyelectrolyte surfaces in oil. Angew. Chem. Int. Ed. 55, 15017-15021 (2016).

[19]Higaki, Y., Inutsuka, Y., Sakamaki, T., Terayama, Y., Takenaka, A., Higaki, K., Yamada, N. L., Moriwaki, T., Ikemoto, Y. & Takahara, A. Effect of charged group spacer length on hydration state in zwitterionic poly (sulfobetaine) brushes. Langmuir, 33, 8404-8412 (2017).

[20]Kobayashi, M., Terayama, Y., Kikuchi, M. & Takahara, A. Chain dimensions and

surface characterization of superhydrophilic polymer brushes with zwitterion side groups. Soft Matter, 9, 5138-5148, (2013).

[21] Murakami, D., Kobayashi, M., Moriwaki, T., Ikemoto, Y., Jinnai, H. & Takahara, A. Spreading and structuring of water on superhydrophilic polyelectrolyte brush surfaces. Langmuir, 29, 1148-1151(2013).

[22] Brown, P. S. & Bhushan, B. Mechanically durable, superoleophobic coatings prepared by layer-by-layer technique for anti-smudge and oil-water separation. *Sci. Rep.*, **5**, 8701, (2015).

[23] Brown, P. S. & Bhushan, B. Bioinspired, roughness-induced, water and oil super-philic and super-phobic coatings prepared by adaptable layer-by-layer technique. *Sci. Rep.*, **5**, 14030, (2015).

[24] Tian, Y.; Jiang, L., Wetting: intrinsically robust hydrophobicity. *Nat Mater*, ***12*** (4), 291-2, (2013).

[25] Ko, T.-J., Oh, K. H. & Moon, M.-W. Plasma-induced hetero-nanostructures on a polymer with selective metal co-deposition. *Adv. Mater. Interfaces*, **2**(1), 1400431, (2015).

[26] Kolev, V. L., Kochijashky, I. I., Danov, K. D., Kralchevsky, P. A., Broze, G. & Mehreteab, A. Spontaneous detachment of oil drops from solid substrates: Governing factors. *J. Colloid Interface Sci.*, **257**(2), 357-363, (2003).

[27] Dodds, S., Carvalho, M. & Kumar, S. Stretching liquid bridges with moving contact lines: The role of inertia. *Phys. Fluids*, **23**(9), 092101, (2011).

[28] Kim, S. J., Kim, S. & Jung, S. Extremes of the pinch-off location and time in a liquid column by an accelerating solid sphere. *Phys. Rev. Fluids*, **3**(8), (2018).

[29] He, B., Lee, J. & Patankar, N. A. Contact angle hysteresis on rough hydrophobic

surfaces. *Colloids Surf., A*, **248**(1-3), 101-104, (2004).

[30] McHale, G., Shirtcliffe, N. & Newton, M. Contact-angle hysteresis on super-hydrophobic surfaces. *Langmuir*, **20**(23), 10146-10149, (2004).

[31] Quéré, D. Wetting and Roughness. *Annu. Rev. Mater. Res.*, **38**(1), 71-99, (2008).

[32] Liu, K., Yao, X. & Jiang, L. Recent developments in bio-inspired special wettability. *Chem Soc Rev*, **39**(8), 3240-55, (2010).

[33] Hejazi, V., Nyong, A. E., Rohatgi, P. K. & Nosonovsky, M. Wetting transitions in underwater oleophobic surface of brass. *Adv Mater*, **24**(44), 5963-6, (2012).

[34] Vourdas, N., Tserepi, A., Stathopoulos, V., Reversible pressure-induced switching of droplet mobility after impingement on porous surface media. *Appl. Phys. Lett.*, **103**(11), 111602, (2013).

[35] Vourdas, N., Ranos, C. & Stathopoulos, V. N. Reversible and dynamic transitions between sticky and slippery states on porous surfaces with ultra-low backpressure. *RSC Adv.*, **5**(42), 33666-33673, (2015).

[36] Vourdas, N., Pashos, G., Kokkoris, G., Boudouvis, A. G. & Stathopoulos, V. N. Droplet Mobility manipulation on porous media using backpressure. *Langmuir*, **32**(21), 5250-8, (2016).

[37] Yoon, R. H. & Yordan, J. L. The critical rupture thickness of thin water films on hydrophobic surfaces. *J. Colloid Interface Sci.*, **146**(2), 565-572, (1991).

[38] Sharma, A. & Ruckenstein, E. Stability, critical thickness, and the time of rupture of thinning foam and emulsion films. *Langmuir*, **3**(5), 760-768, (1987).

[39] Coons, J. E., Halley, P. J., McGlashan, S. A. & Tran-Cong, T. Scaling laws for the critical rupture thickness of common thin films. *Colloids Surf., A*, **263**(1-3), 258-266, (2005).

Chapter 3. Transparent and highly adhesive hydrogel coated polyethylene terephthalate (PET) for anti-oil fouling

3.1. Introduction

Recently, the demand for underwater superoleophobic surfaces with excellent superhydrophilicity has increased in various application fields, such as anti-oil fouling, oil-water separation, and biosensors [1-5]. Underwater superoleophobicity can be achieved through the combination of surface roughness and the hydrophilic nature of a coating or material. However, most underwater oleophobic surfaces are opaque or semitransparent based on light scattering caused by surface structures, which limits their application to underwater optical devices, such as underwater cameras, diving goggles, and imaging substrates for biologically active cells or tissues [6]. To date, there have only been a few studies on transparent underwater oleophobic surfaces made of transparent ceramics (e.g., glass or sapphire). Naureen et al. fabricated a transparent underwater oleophobic surface from miscut (0001) sapphire [7] and Jiale et al. performed nanoscale ablation on silica glass utilizing femtosecond laser treatment [6]. Thomas et al. fabricated an oil-repellent wastewater optical sensor from nano-rough surfaces with an ultrathin fluoropolymer coating layer [8] and Yunjiao et al. fabricated a poly(vinyl alcohol)/silica coating on glass as an underwater superoleophobic layer [9]. However, studies on transparent underwater oleophobic surfaces utilizing

synthetic polymers have rarely been reported based on the intrinsic hydrophobicity and smooth surfaces of such materials. For several decades, polyethylene terephthalate (PET) has been widely used on optical devices based on its excellent optical transmittance (89.0%) and various other advantages, including chemical and physical durability, low cost, flexibility, stability, softness, lightness, elasticity, and anti-wrinkling properties [10]. Despite these advantages, PET has received little attention in the fields of anti-fouling, biomaterials, and printing, which require robust hydrophilicity. A few surface treatment methods have been applied to PET to induce hydrophilicity, including plasma treatment, colloidal lithography, and surfactant-based coating [11-13]. Plasma treatment is actively used as a generalized, fast, and adjustable approach for modifying various types of plastics [14-15]. However, it has been reported that the robustness of plasma-induced hydrophilicity on PET surfaces is very weak due to aging or hydrophobic recovery behaviors [16-19].

To prolong the wettability of hydrophilic treated surfaces, some functional hydrophilic layers, such as hydrogel layers, have been applied to resist hydrophobic recovery [20]. Hydrogel is a popular material in various fields, including anti-fouling, oil-water separation, and medical devices, based on its excellent hydrophilicity, biocompatibility, chemical stability, adjustable mechanical strength, elasticity, and transparency [21-22]. In particular, there have been many studies on anti-oil fouling based on the hydrophilic characteristics of hydrogel, which consists of a cross-linked network with water-filled interstitial

spaces [23-24]. However, strong adhesion between hydrogel and substrate hardly be achieved due to its unique feature, therefore, most hydrogel coating studies have focused on increasing the interfacial adhesion strength between solids and hydrogel [25-26]. It is known that hydrogel coating approaches require radical grafting on surfaces, such as oxygen plasma treatment or aminolysis processing, to increase chemical bonding to improve adhesion strength on hydrophobic surfaces [24]. But, up-to-date, interfacial strength based solely on chemical bonding may not be sufficient for maintaining a hydrogel coating on target surfaces for either air or water environments.

In this paper, we proposed a mechanically interlocked hydrogel (polyacrylamide, PAAm) coating on transparent PET polymer for robust anti-oil fouling applications. We adopted plasma-induced high-aspect-ratio nanostructures (HARns) to form mechanical interlocking between the hydrogel and substrate to achieve strong interfacial adhesion [26-28]. A highly adhesive hydrogel coating was deposited onto a non-porous hydrophobic PET surface following one-step selective etching oxygen plasma treatment without any pretreatment. Conventional oxygen plasma treatment is known to alter only surface chemistry, whereas oxygen plasma treatment with selective etching not only induces chemical changes, but also nanostructure formation, which further enhances the interfacial adhesion strength between the hydrogel and PET substrate. The morphology of the plasma-induced HARns can be controlled by the tuning plasma treatment duration and gas species [29], allowing precise control of their aspect ratios. Because the hydrogel

coating can penetrate between the nanostructures, the contact area for bonding is increased through mechanical interlocking between the hydrogel and HARn PET surface. The mechanically interlocked hydrogel layer on the nanostructured PET exhibits much higher adhesion strength than that on the pristine PET, enabling the underwater application. Also, our proposed hydrogel-coated polymer renders extreme wettability and superhydrophilicity in air, as well as excellent underwater oleophobicity, while maintaining optical transparency. As shown in the left image in Fig. 3.1a, the hydrogel layer coated onto the pristine PET surface (without treatment) is spontaneously peeled off in water based on swelling following water absorption [30]. In contrast, the hydrogel coated onto the HARn surface remains firmly adhered after swelling based on enhanced adhesion (right image in Fig. 3.1a). Optical transmittance is reduced by the light scattering based on surface roughness following nanostructure fabrication. However, it recovers following hydrogel coating because the optical refractive index of hydrogel is well matched to that of PET. Finally, we demonstrate anti-oil fouling with high transparency in an underwater camera protector submerged in crude-oil-covered water. When PET-mounted cameras were dipped into the crude-oil-covered water, the pristine PET-mounted camera lens was completely fouled by crude oil. In contrast, the lens mounted on the PAAm-coated HARn PET clearly maintains its transparency, as shown in Fig. 3.1b.

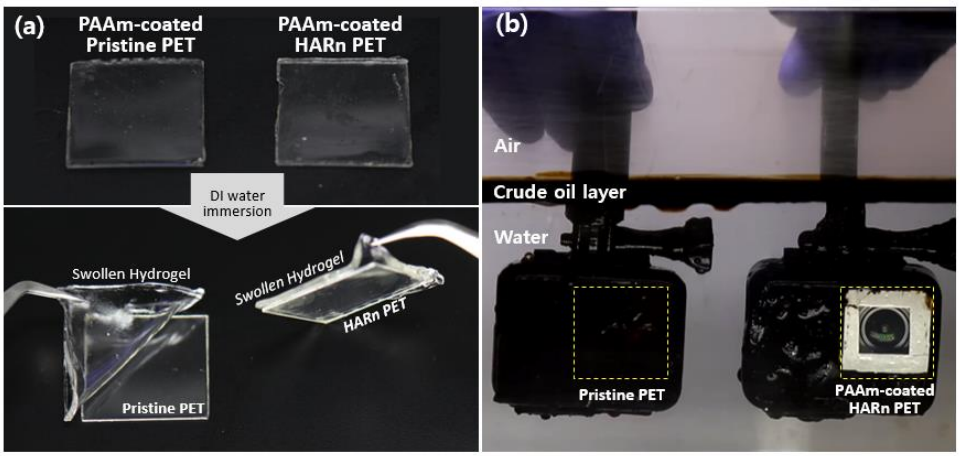

Fig. 3.1 Research overview of coating adhesion and anti-oil fouling. (a) Optical images showing a comparison of hydrogel coating adhesion onto pristine PET (left) and HARn PET (right) following 2 h of deionized (DI) water immersion with stirring. (b) Images of underwater camera protectors dipped in crude-oil-covered water utilizing pristine PET (left) and PAAm-coated HARn PET (right). Rectangular dotted boxes represent the regions with PET covers.

To investigate interfacial toughness decreasing under swelling effect, we performed the additional immersion and stirring (1150 rpm) test. The hydrogel, coated on pristine PET was spontaneously detached from the surface after 2hours the DI water immersion and stirring test. On the other hands, the hydrogel, coated on HARn PET adhered to the surface after 3days but it also easily peeled off. (See Fig. 3.2) The most hydrogel's interfacial toughness is decrease when it contact aqueous solution as swelling effect. Chen et al., investigated the decreased interfacial toughness upon swelling, the intrinsic bulk toughness decreases due to the swelling induced network deformation. Thus, the swelling-induced bulk gel deformation leads to a lower measured interfacial toughness after soaking in aqueous solution.

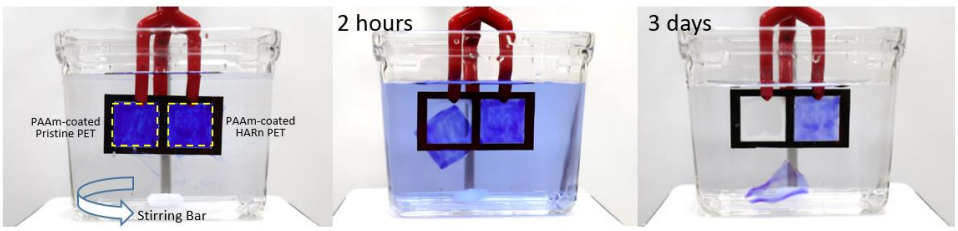

Fig. 3.2 Immersion and stirring test of hydrogel, coated on pristine PET (left) and HARn PET (right). The hydrogel on pristine PET, spontaneously peeled off after 2 hours. On the other hands, the hydrogel on HARn PET, adhered on the surface after 3 days.

3.2. Materials and Methods

3.2.1. Materials

PET transparent films were purchased from a local company (Sehan Co., South Korea). The samples were cut to dimensions of 30 × 30 × 0.1 mm. The PAAm hydrogel coating was fabricated utilizing the following procedure [31]. First, 10 g of acrylamide was dissolved in DI water (40 mL) and stored at 4 °C for 1 h to obtain a 20 wt% homogeneous solution. Next, 0.1 M of N,N-methylenebisacrylamide and N,N,N',N'-tetramethylethylenediamine were added as a crosslinker and a crosslinking accelerator for PAAm, respectively. Then, 0.2 M of ammonium persulphate was added as a radical initiator for PAAm. A uniformly distributed acrylamide solution was poured onto the substrate and cured under ultraviolet (UV) light (8 W of power and 254 nm wavelength) for 1 h prior to stabilization at room temperature for 2 d.

3.2.2. Surface modification of the PET film

The HARn PET film was fabricated via one-step selective oxygen plasma etching utilizing a custom plasma etching device with a plasma power and substrate bias voltage of 230 W and 400 V, respectively. With an oxygen gas flow rate of 40 sccm, the plasma treatment duration was varied from 5 to 60 min, resulting in various aspect ratios of nanostructures, which are defined by the ratio of the height to the diameter. The aspect ratios ranged from 1.7 to 26.8. Here, HAR is defined as a ratio greater than 18, which provides strong interfacial bonding

between the solid and hydrogel. Note that under normal plasma treatment conditions, protecting the PET from metallic element deposition for selective plasma etching for nanostructure formation was performed to achieve a PET surface that is smooth, but hydrophilic [12]. The prepared acrylamide solution was poured onto the HARn PET and cured under UV light (8 W of power and 254 nm wavelength) for 1 h prior to stabilization at room temperature for 2 d. Three different thicknesses of PAAm were prepared as a thin PAAm film (approximately 500 nm, rough surface), thick PAAm film (approximately 100 μm, smooth surface), and very thick PAAm film (approximately 2 mm, prepared for peel testing) for coating onto the HARn PET surface. The fabricated HARns and PAAm-coated HARn PETs were aged at 110 °C for 72 h to evaluate the effects of hydrophobic recovery.

3.2.3. Surface characterization

Surface morphology was explored utilizing scanning electron microscopy (SEM, Inspect F, FEI, US) with a 10 kV acceleration voltage. A 6-nm-thick Pt layer was deposited onto the sample surfaces to provide better conductivity and prevent electron charging. The chemical composition of fabricated surfaces was investigated utilizing X-ray photoelectron spectroscopy (XPS, K-ALPHA, Thermo Fisher Scientific, UK), with measurement parameters of 12 kV, 6 mA, and 72 W. Surface hydrophilicity and underwater oleophobicity were quantified based on water contact angle (WCA) and underwater oil contact angle (OCA) measurements, respectively. WCA measurement was performed utilizing a

goniometer (Rame-Hart, Model100, US) in ambient air at 20 °C with a relative humidity in the range of 25–40%. OCA was recorded by a digital camera (EOS 60D, Canon, Japan) in underwater conditions with crude oil (Hyundai Oil Bank Co. South Korea) droplets with a volume of 5.0 ± 0.5 μl. Real-time underwater anti-oil fouling behavior was recorded by a water-proof action camera (GoPro HERO5, US). The topography of the surface was measured utilizing atomic force microscopy (AFM, XE-70, Park systems Co., South Korea) in non-contact mode with an area of 10 × 10 μm. The optical transmittance of each PET substrate was evaluated utilizing a UV-visible spectrophotometer (V-730, Jasco Inc., USA) with a wavelength range of 300–900 nm.

3.2.4. Measurement of coating adhesion

The T-peeling test (ASTM D1876) method was applied for peel testing to evaluate the interfacial adhesion of the hydrogel coating. Tensile testing of the hydrogel was performed utilizing a universal material tester (Exceed model E42, MTS, US). A rigid polyvinyl chloride (PVC) back plate with a thickness of approximately 100 μm was attached to the surface of the hydrogel sheet to prevent elongation of the hydrogel along the peeling direction. The measured interfacial toughness is equal to the steady-state peeling force per unit width of the hydrogel sheet [24].

3.3. Results and discussion

3.3.1. Surface modification

A pristine PET film is transparent, hydrophobic, and non-porous, making it difficult to deposit a durable and uniform hydrogel coating on the PET surface. To deposit a robust hydrogel coating, the surface of PET must be modified to generate hydrophilicity and the roughness must be increased to enhance interfacial bonding. Highly adhesive surfaces were generated utilizing the surface treatment process presented in Fig. 3.3. Selective oxygen plasma etching was applied to pristine flat PET for 30 min (Fig. 3.3(a)). During the plasma process, it is known that hydroxyl polar functional groups are implemented into the PET surface (generating hydrophilicity) [16]. Additionally, nanostructures with HARs are also created by oxygen plasma etching. The formation mechanism of HARns is that metal particles are sputtered from the stainless steel cathode plate, then co-deposited on the PET surface, forming metal nano-islands during plasma treatment. These metal particles act as an etching mask and covered regions exhibit low etching rates. Regions where these metal particles are not deposited exhibit a high etching rate based on rapid chemical reactions between oxygen plasma ions and the hydrocarbon polymeric surface. Therefore, HARns are eventually generated with a long treatment duration [12, 32-33]. Fig. 3.3(b) presents a HARn surface after 30 min of oxygen plasma treatment. One can see well-developed nanostructures with a HAR of 18.9. Fig. 3.7 presents the surface evolution as oxygen plasma duration increases. The aspect ratios increase from 1.7 to 26.7 as

the duration increases from 5 to 60 min, but the structure density decreases after 30 min of treatment based on the agglomeration of nanostructures [34].

The acrylamide solution was poured onto the HARn PET with an AR of 18.9 for hydrogel coating. The thickness of the coating layer was controlled by the volume of solution in a range from thin (approximately 500 nm, solution volume ≈ 0.05 μl/cm2) to thick (> 100 μm, solution volume > 10 μl/cm2). Fig. 3.3(c, left) presents a thin PAAm-coated HARn PET sample, which reflects nanoscale roughness from the nanostructures of the PET onto the hydrogel-covered surface as nano-bumps. In contrast, the thick PAAm-coated surface in Fig. 3.3(c, right) has a relatively smooth surface, which only reflects the hydrogel surface roughness. The measured roughness values (Rq, root-mean-squared average) of the thin and thick coating surfaces based on AFM (Fig. 3.4) are 20.94 and 1.42 nm (similar to the value for pristine hydrogel of approximately 1.9 nm) [35], respectively, indicating that only the thin PAAm-coated HARn PET surface has nanoscale surface roughness. Note that the nanostructures on the thin PAAm-coated HARn PET have relatively larger diameters than those on the uncoated HARn PET because the nanoscale hairy structures can merge into nanoscale clusters during hydrogel coating.

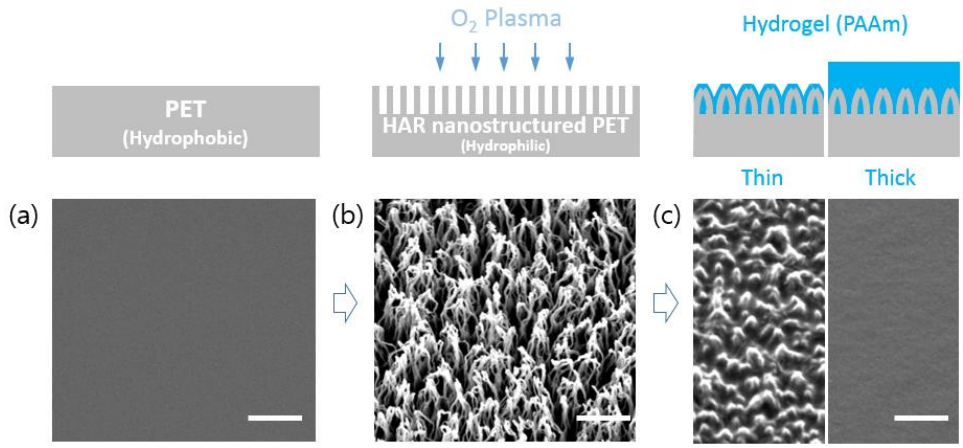

Fig. 3.3 Schematic and SEM images of the nanostructuring process utilizing one-step selective oxygen plasma etching and a subsequent hydrogel coating on HARn PET. (a) The pristine PET film, (b) HARn-PET (b), and (c) PAAm-coated HARn-PET with coating thicknesses of 500 nm (thin, left) and 100 μm (thick, right). Scale bars are 1 μm.

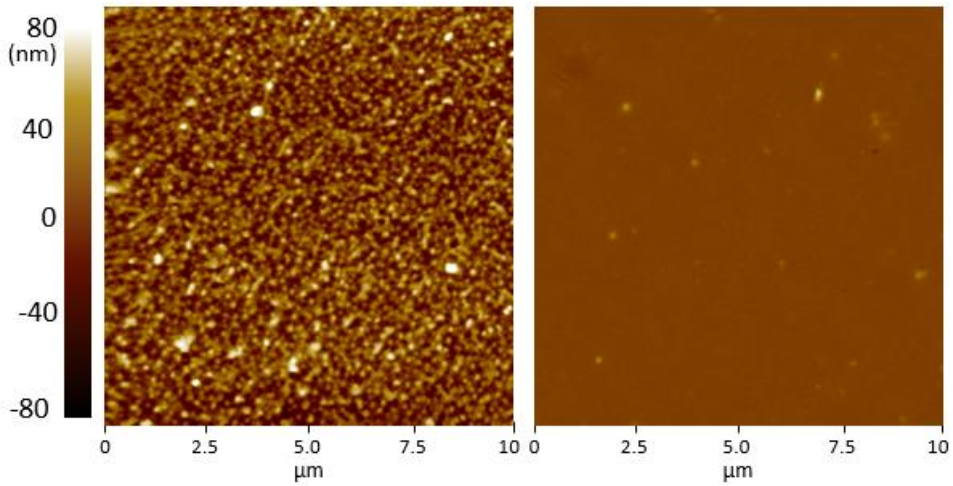

Fig. 3.4 Atomic force microscopy images of the topographies of hydrogel-coated surfaces. (a) Thin PAAm-coated HARn PET with 500 nm coating thickness. (b) Thick PAAm-coated HARn PET with 100 µm coating thickness.

3.3.2. Hydrophilicity and underwater oleophobicity of PET with wettability aging

Surface wettability is a crucial factor for anti-oil fouling properties. It is known to be governed by two components of a solid surface, namely chemical composition and geometrical structure [36-38]. Selective oxygen plasma etching is regarded as a facile one-step process for optimizing these two features to increase roughness and hydrophilicity. During oxygen plasma etching, hydroxyl functional groups, which have a hydrophilic nature, are adopted, causing surface properties to transform from hydrophobicity to hydrophilicity. Surface roughness is also increased by nanostructure formation based on the selective oxygen plasma mechanism [12]. We performed contact angle measurements to quantify the hydrophilicity in air and underwater oleophobicity for each surface. Four types of samples were prepared, namely pristine, HARn, thin PAAm-coated, and thick PAAm-coated HARn PETs. It is known that hydrophilicity induced via surface treatment can be recovered to the intrinsic wettability of materials based on the diffusion of implemented functional groups or contamination by airborne hydrocarbons or moisture. To determine the aging behavior of each sample, all samples were placed in a furnace at 110 ℃ for 72 h to accelerate the aging process [33, 39]. The WCAs in air and underwater OCAs with crude oil are presented in Figs. 3(a) and 3(b), respectively. The WCA of the pristine PET is unchanged at 83.4 ± 1.4°, regardless of thermal aging, whereas the WCA of the HARn PET without a PAAm coating is significantly increased by aging-induced

hydrophobicity recovery from superhydrophilicity (16.4 ± 8.9°) to hydrophobicity (86.0 ± 4.1° after 2 h of aging) and superhydrophobicity (164.7 ± 2.6° after 3 d of aging). It should be noted that once the hydrophobic nature of PET is recovered after aging, the nanostructured PET surface exhibits superhydrophobicity based on hydrophobic nanostructures in the Cassie-Baxter state [33]. For the PAAm-coated HARn PET, the surface exhibits a low WCA based on the hydrophilic nature of PAAm hydrogel. The WCAs of the thin and thick PAAm-coated HARn PETs were measured to be 15.5 ± 2.1° (superhydrophilicity) and 32.1 ± 12.4° (hydrophilicity), respectively. These values remained stable after 72 h of aging. The difference between the WCAs of the thin and thick PAAm-coated surfaces stems from a significant difference in surface roughness [40]. As shown in Fig. 3.3(c, left), the thin PAAm-coated HARn PET reflects the nanoscale roughness of the HARn PET, which enhances its hydrophilicity, while the thick PAAm-coated HARn PET has a relatively smooth surface (Fig. 3.3(c, right)), providing the same hydrophilicity as the hydrogel.

Fig. 3.5(b) presents the OCAs of each sample versus aging time. The OCAs of the samples were measured to be 39.6 ± 12.8° for the pristine PET (underwater oleophilicity), 162.4 ± 4.1° for the thin coating, and 161.2 ± 5.5° for the thick coating (underwater superoleophobicity). The OCA values of these samples are all stable, regardless of thermal aging duration. The HARn PET exhibits strong underwater oleophobicity immediately after preparation. However, it transitions to an oleophilic state based on a sharp decrease in the OCA as aging

duration increases. The HARn PET surface after 72 h of aging reaches a stable state of underwater oleophilicity with an OCA of 28.2 ± 0.9°.

To investigate changes in the surface chemical compositions of each sample, XPS analysis was conducted for six different PET surfaces, namely pristine, aged pristine, HARn, aged HARn, PAAm-coated HARn, and aged PAAm-coated HARn PET surfaces. As shown in Figs. 3.5(c–f), C−C, C−O, C=O, and O−C=O groups are prominent in the C1s spectra. Following oxygen plasma treatment on the pristine PET (also on the HARn PET), the atomic composition of C−C groups decreases from 60.8% to 53.3%, while those of oxygen-related C−O and C=O groups increase from 18.3% to 24.6% and 16.8% to 17.3%, respectively. This result was examined in greater detail utilizing elemental composition analysis. The overall carbon composition decreases from 75.8% to 52.9% while the overall oxygen composition increases from 24.2% to 39.1%, indicating that hydroxyl polar functional groups were implanted into the HARn PET surface during oxygen plasma treatment. During aging via annealing at 110 ℃ overall 24 h, the chemical composition of the aged PET (pristine, Fig. 3.5(c)) does not change significantly. However, in case of the aged HARn PET, which suffers from hydrophobicity recovery, the chemical composition changes as follows: C−C from 53.3% to 60.7% and C−O from 24.6% to 20.7%. These changes indicate a reduction of oxygen-related bonds. Previous studies have investigated the mechanisms of the hydrophobic recovery process. When oxygen-plasma-treated surfaces are aged, polar functional groups are buried away from the polymer surface to optimize

surface free energy and eventually return to a hydrophobic state [19, 41]. However, the PAAm-coated HARn PET exhibits no noticeable change in bonding or elemental composition during aging, indicating that the PAAm-based hydrogel is sufficiently stable for thermal aging [42-43].

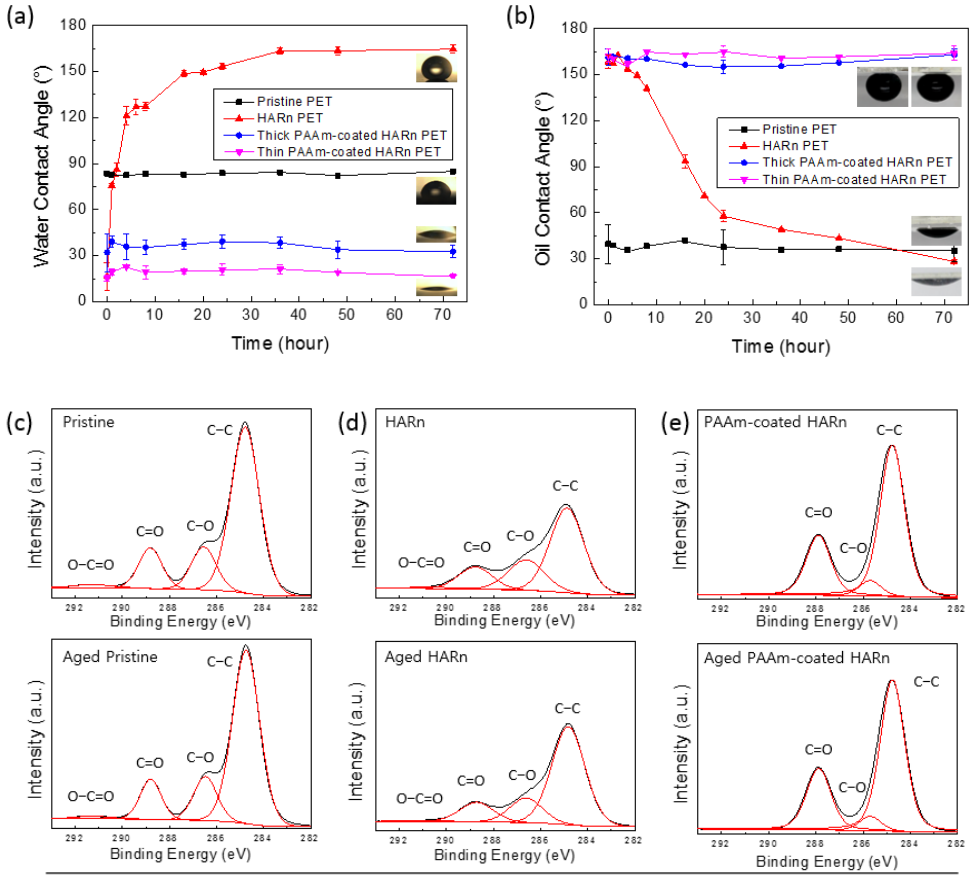

(f)

XPS analysis		Bonding contribution (At%)				Elemental composition (At%)						
		C–C group	C–O group	C=O group	O–C=O group	C	O	N	Si	Ca	Cr	Fe
(C)	Pristine PET	60.8	18.3	16.8	4.1	75.8	24.2	-	-	-	-	-
	Aged pristine PET	61.9	18.2	16.4	3.5	75.5	23.9	-	0.6	-	-	-
(d)	HARn PET	53.3	24.6	17.3	4.9	52.9	39.1	1.0	4.1	0.2	0.9	2.0
	Aged HARn PET	60.7	20.7	14.7	3.9	54.2	36.8	0.9	4.8	0.3	0.9	2.2
(e)	PAAm-coated HARn PET	56.4	20.2	23.4	-	62.0	19.0	18.4	0.6	-	-	-
	Aged PAAm-coated HARn PET	56.2	19.8	23.9	-	61.6	19.0	18.8	0.6	-	-	-

Fig. 3.5 CA measurements in water and oil. The HARn PET exhibits hydrophobic recovery. (a) WCA measured in air. (b) OCA for crude oil underwater. XPS analysis of six surfaces. The upper row presents the non-aged PET results and the lower row presents the thermally aged PET results over 24 h. (c) Pristine PET and aged pristine PET. (d) HARn PET and aged HARn PET. (e) PAAm-coated HARn PET and aged PAAm-coated HARn PET. (f) Table listing the results for total bonding contributions and elemental compositions.

3.3.3. Enhanced hydrogel coating adhesion

We anticipated that the superhydrophilic HARn structures would promote the uniform infusion of the hydrogel solution into the spaces between nanostructures. The attraction between the liquid solution and solid structures should ensure stable gelation, resulting in the enhanced coating adhesion based on increased contact area between the gel and nanostructures. To explore the effects of surface roughness and wetting state on adhesion, we conducted peeling tests on PAAm-coated PET films. PAAm-coated PET samples were prepared with four different surface conditions: a hydrophobic smooth surface (pristine PET), superhydrophobic HARn surface (30 min plasma treated, 1 d thermally aged), hydrophilic smooth surface (30 min normal plasma treated, no aging) and superhydrophilic HARn surface (30 min selective etching plasma treated, no aging). Next, a thin PVC film backing was attached to the bottom of the PAAm sheets to prevent elongation in the peeling direction. The measured interfacial toughness is equal to the steady-state peeling force per unit width of hydrogel sheet [44]. Fig. 3.6(a) presents an overview of the T-peeling test in a schematic form. The PAAm hydrogel with a PVC film backing is fixed on the lower load cell to minimize self-load interference. The PET, which thoroughly cut off from the interface between PET and the PAAm hydrogel, is fixed to the upper load cell. Peeling tests were conducted with a peeling rate of 2 mm/min to measure interfacial toughness. Note that the hydrogel contained approximately 80 wt% of water. Fig. 3.6(b) presents comparative results for the PAAm-coated HARn PET

(hydrophilic rough surface, red line) and pristine PET (hydrophobic smooth surface, black line). The upper row (red doted box) of images reveals PAAm residues attached to the surface of the peeled HARn PET, indicating that the HARn surface provides greater adhesion strength compared to the cohesion strength of the hydrogel itself (approximately 163 N/m) [45-46] The image of the peeling interface between the HARn PET and PAAm hydrogel sheet reveals that the hydrogel is stuck on the interface and elongated on the HARn surface (Fig. 3.6b). However, there is no residue on the side of the hydrophobic PET and clean debonding can be observed at the interface (bottom images in Fig. 3.6b). The lower row (yellow outline) of images reveals a clean surface, indicating that the smooth surface has a lower adhesion strength compared to the cohesion strength of the hydrogel itself. After peeling, the pristine PET surface shows no hydrogel residue, as indicated by the yellow outlines highlighting optical and SEM images. The measured interfacial toughness is 13.3 N/m for the smooth hydrophobic PET in the orange dashed line in Fig 3.6(c), which is similar to the value reported in a previous study for a flat glass [24]. In the case of the simple plasma-treated PET with no HARn (hydrophilic), the interfacial strength is improved to as much as 83.2 N/m, while the average value for the superhydrophilic HARn PET surface is 149.3 N/m, as indicated by the green lines. This value is as much as 11 times greater than the values for the pristine PET, indicating the contribution of mechanical interlocking on enhancing interfacial adhesion. Note that the measured value for the aged-HARn PET with a hydrophobic interface is lower than that for superhydrophilic

PET. The curves of peeling force also reveals differences between the pristine and HARn surfaces. Fig. 3.6(c) presents the curve of the pristine sample, which smoothly reaches a steady-state at approximately 13.3 N/m without fluctuation. In contrast, the curves of the HARn samples exhibit a saw-tooth pattern that increases steeply to the maximum peeling force of 259.79 N/m, then drops steeply to 123.18 N/m as the hydrogel is elongated and broken at the interface. This behavior of hydrogel elongation and breaking is repeated until the hydrogel is fully detached from the PET. The hydrophobic HARn surface (Fig. 3.6(c) blue line) and hydrophilic smooth surface (Fig. 3.6(c) pink line) also exhibit similar elongation and breaking behaviors, but with relatively low adhesion forces (65.1 N/m and 83.2 N/m, respectively) compared to that of the superhydrophilic HARn surface. Fig. 3.8(a) presents a schematic of the anticipated interfaces between the hydrogel coating and target PET surfaces with various chemical and mechanical characteristics. The PAAm solution has difficulty penetrating to the bottom of the aged HARn surface based on hydrophobic wetting properties, which prevent stable contact between the solution and nanostructured solid interface. In contrast, the hydrophilic smooth surface treated with mild oxygen plasma (roughness of 30 nm) has increased surface reactivity based on the grafting of hydroxyl functional groups, which generate hydrogen bonds with PAAm hydrogel solutions during gelation. This difference in surface chemical composition leads to the different values for adhesion strength between smooth surfaces with different levels of wettability.

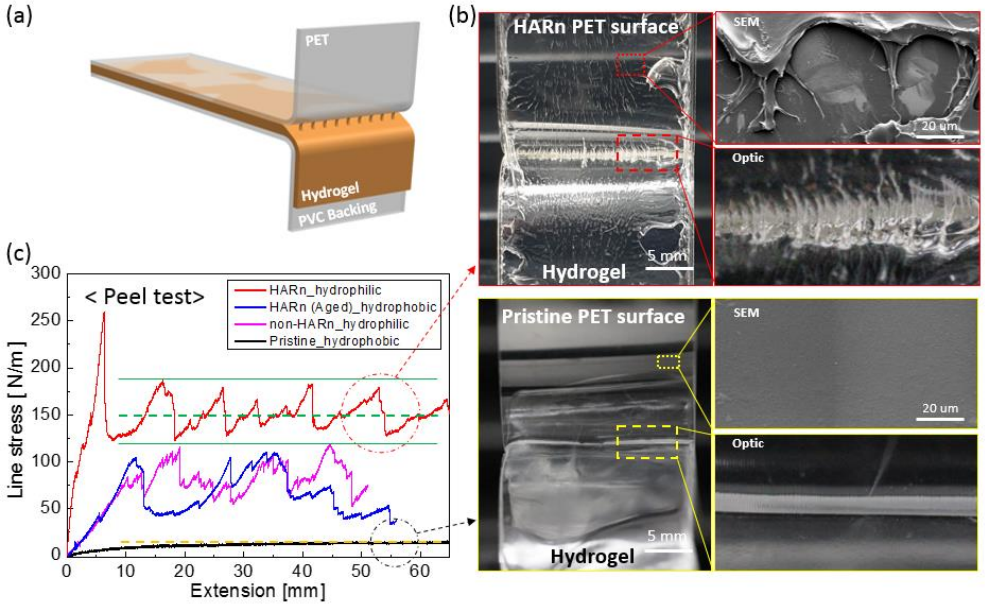

Fig. 3.6 The T-peeling test results for pristine and HARn PET surfaces with hydrogel-solid bonding. (a) Peeling test overview. (b) Peel-tested surfaces of PAAm-coated HARn and pristine PET. Upper row (red) images present the peeled HAR PET surface. (c) Curves of peeling force per unit width of PAAm versus pristine (smooth, hydrophobic), non-HARn (smooth, hydrophilic), HARn (rough, hydrophilic), and aged-HARn (rough, hydrophobic) PET surfaces.

To explore the changes in hydrogel coating adhesion based on surface roughness, we conducted additional experiments to investigate the effects of nanostructure AR on adhesion strength. PET films were prepared under five different sets of treatment conditions with oxygen plasma treatment durations of 5, 10, 20, 30, and 60 min. The corresponding ARs of the resulting nanostructures were 1.7, 6.5, 15.7, 18.9, and 26.7, respectively (see Fig. 3.7).

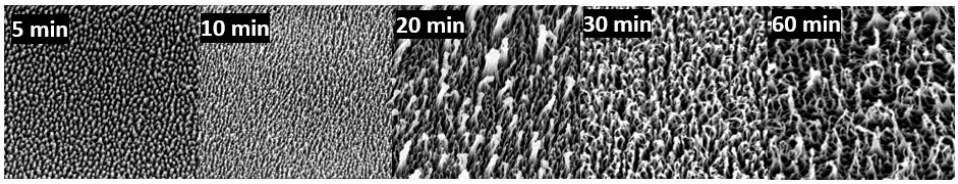

Fig. 3.7 Evolution of nanostructures as oxygen plasma duration increases.

The average measured values of interfacial strength in the peeling tests were 81.4, 87.8, 104.3, 149.1, and 111.0 N/m, respectively (Fig. 3.8(b)). As the surface AR increases, the adhesion force also increases up to certain level, then decreases with treatment times longer than 30 min based on the reduction of HARn density, as shown in Fig. 3.8.

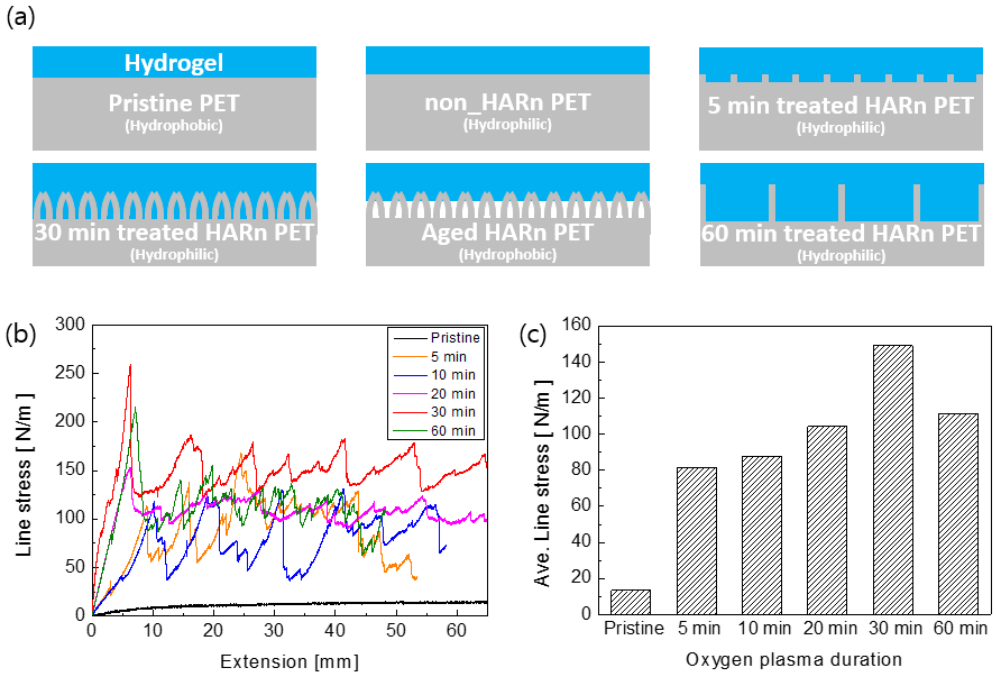

Fig. 3.8 (a) Schematics of hydrogel coating morphologies as surface roughness and characteristics change. (b) T-peeling test results as surface roughness and plasma treatment duration increase. (c) Average measured stress.

The AR of HARn was increased as the plasma treatment duration increased, but the HARn structures were aggregated after certain level due to the Van der Waals force shown in Fig. 3.9. But the aggregated HARn that exposed the flank side, were eliminated by oxygen plasma etching due to the regions did not protected, only the central HARn which had normal direction etching mask remains. Eventually, the HARn density was decreased.

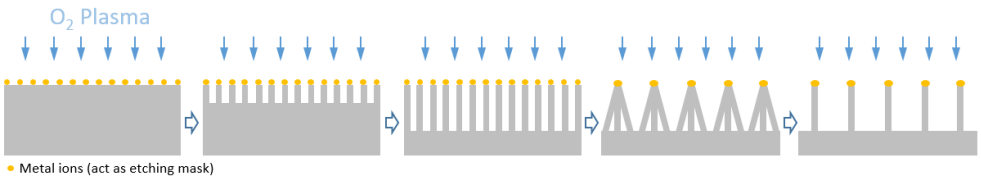

Fig. 3.9 The schematic of decrease of HARn density as the selective-etching oxygen plasma duration increase.

3.3.4. Optical transmittance of modified surfaces

Optical transparency is a very important factor for optical devices and is known to be significantly affected by surface roughness. As discussed earlier, a rough surface structure increases wettability characteristics, such as superhydrophilicity in air and underwater superoleophobicity, but rough surfaces are typically opaque because of light scattering caused by roughness, especially nanoscale roughness [6]. We prepared four types of samples for transmittance testing, namely pristine, HARn alone, and thin and thick PAAm-coated HARn PET. Fig. 3.10(a) presents the transmittance curves of PET samples with different surface conditions. The transmittance of the HARn PET with oxygen plasma treatment for 30 min drops to 65.1% in the violet area (400 nm wavelength, value for pristine PET is 85.0%) based on the increased light scattering caused by the HARn structures [34]. However, the transmittance values of the HARn PET samples coated with thin and thick PAAm hydrogel recover to 84.7 and 84.2%, respectively, which are similar to the original value for the pristine PET film. The underlying mechanism for the recovery of transmittance via hydrogel coating on nanostructured surfaces is similar to a natural phenomenon where the petals of Diphylleia grayi become transparent in the rain [47]. When light beams pass through the interface between two different materials, very little refraction occurs if the two materials have similar refractive indices [6]. The refractive index of the PAAm hydrogel ($n_{PAAm} \approx 1.51$ at 20 ℃) [48], which fills the spaces between HARn structures, is closer to the index of pristine PET ($n_{PET} \approx 1.59$ at 20 ℃)

[49] than it is to the index of air (n air ≈ 1.00 at 20 ℃) [50]. As the hydrogel fills the spaces between nanostructures, it firmly holds the structures on the HARn PET. Fig. 3.10(b) presents the transparency and wetting behaviors of each surface. The pristine PET is transparent, but water drops reveal a hydrophobic nature with a WCA of 83.4 ± 1.4°. The HARn PET is slightly opaque or semi-transparent with superhydrophilicity based on the HAR of the roughness and hydrophilic nature induced by oxygen plasma treatment. The PAAm-coated HARn PETs are transparent with superhydrophilicity, regardless of the thickness of the coating layer.

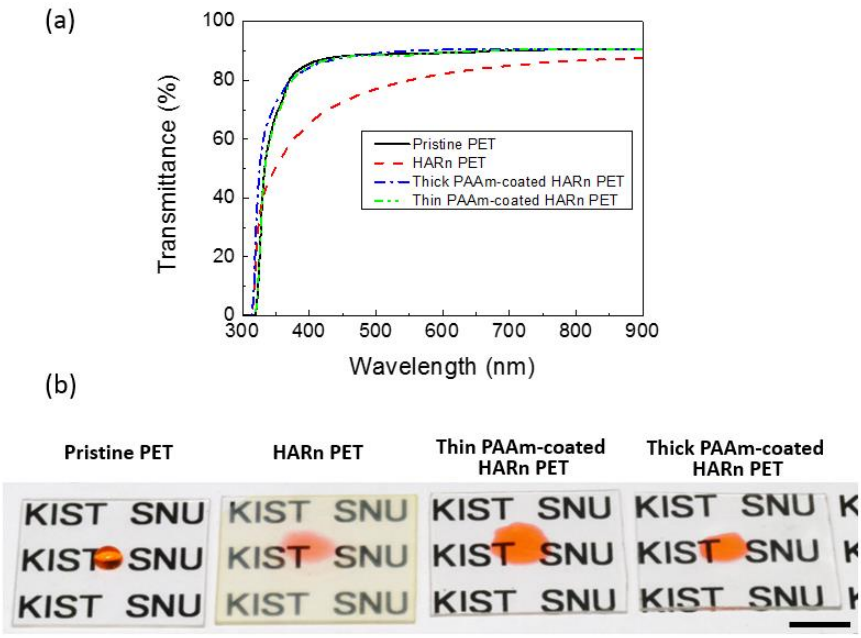

Fig. 3.10 (a) Transmittance of prepared PETs with and without hydrogel coating. (b) Optical images of the pristine (left), HARn (middle), and thin/thick PAAm-coated HARn PET (right) samples. Water was dyed red and the scale bar is 10 mm.

3.3.5. Application to underwater optical sensor protection and scratch durability

For demonstrative purposes, we applied PAAm-coated HARn PET as a protective window for an underwater camera or underwater optical sensor system to facilitate oil-fouling-free operation in oily water. Prior to the demonstration, we explored the oil repellency of each type of PET surface. Five samples were prepared with pristine, HARn, aged HARn, PAAm-coated HARn, and aged PAAm-coated HARn PET. The samples were temporarily immersed in DI water for 1 s to pre-wet each surface. Crude oil was then deposited on each surface with a volume of 10 μl in air. Water was then poured onto the oil-fouled-PET surfaces, as shown in Fig. 3.11. The crude oil residues on the pristine PET and aged HARn PET remained on these surfaces based on their relatively high oil affinity, whereas the HARn PET (not aged), PAAm-coated HARn PET, and aged PAAm-coated HARn PET samples exhibited excellent oil removal performance and were cleaned immediately on contact with water.

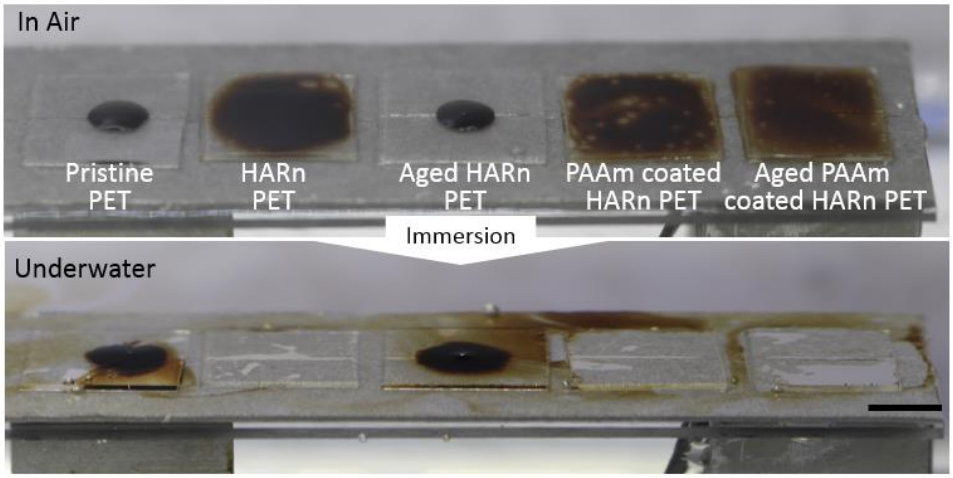

Fig. 3.11 Crude oil fouling and removal from prepared PET surfaces. Scale bar is 10 mm.

For the optical device application in an oily water environment presented in Fig. 3.12, various types of surfaces were prepared, namely plain glass and pristine, HARn, aged HARn, PAAm-coated HARn, and aged PAAm-coated HARn PET. The samples were mounted on camera lenses and pre-wetted via spraying with DI water in air, then immersed in oily water, as shown in Fig. 3.12(a). Fig. 3.12(b) presents optical images captured through the camera lenses during immersion tests. The top row contains images captured prior to immersion. The hydrophilic glass (WCA ≈ 30°) and mildly hydrophobic pristine PET (WCA ≈ 65°) yield partially opaque images (red arrow) because the water drops are not spread out, resulting in the formation of fog droplets, which reflect light randomly. The hydrophilic surfaces (HARn PET without aging and hydrogel coated samples) yield clear images based on their low WCAs (approximately 16.4°) because the water drops spread out uniformly. The bottom row contains images captured underwater through the PET covers, which passed through the crude oil layer on the water. The glass and pristine PET are fouled by crude oil, except in the regions with water droplets (indicated by the red arrows in the upper row). The HARn PET maintains a clean and transparent surface, demonstrating anti-oil fouling properties. However, the aged HARn PET is fouled by crude oil based on hydrophobic recovery, which prevents the nanostructured PET from being wetted by water. In contrast, the PAAm-coated PET maintains its clean and transparent surface, regardless of aging, even with cyclic immersion tests. Fig. 3.12(c) presents the results for the surface cleaning rate of each sample. These results were obtained by

measuring the area ratio of oil-free regions. It was determined that the glass, pristine PET, and aged HARn PET are easily fouled by crude oil, whereas the HARn PET, PAAm-coated PET, and aged PAAm-coated PET maintain clean surfaces with cleaning rates close to 100%, indicating oil-free surfaces.

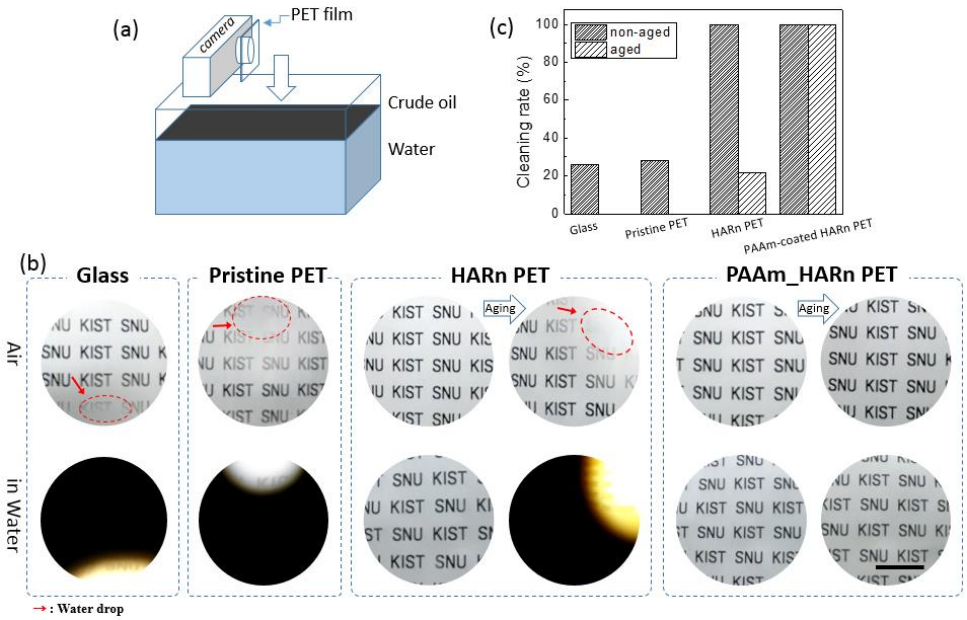

Fig. 3.12 Results for underwater camera protectors in crude-oil-covered water utilizing various surfaces. (a) Schematic of the immersion experiment. (b) Optical images of the samples before (upper row) and after (lower) water immersion testing. (c) Cleaning rates of various surfaces underwater. Scale bar is 10 mm.

To explore anti-oil fouling and transparency following physical damage, we conducted a scratch test on the thick coated PAAm PET surface. The experimental procedure was the same as that for the previous immersion test, as shown in Fig. 3.13(a). We prepared two different hydrogel-coated PET surfaces with scratch depths of approximately 0.15 and 0.40 mm utilizing a razor blade (Fig 3.13(b)). The as-prepared surfaces were mounted to a camera lens and immersed in crude-oil-covered water. In the upper row of images in Fig. 3.13(c), the samples are opaque in air based on the depth of scratches cut into the hydrogel. The shallow scratched (approximately 0.15 mm) surface is only partially unclear, whereas the deep scratched (approximately 0.40 mm) surface results in more opaque images. The lower row of images are underwater images captured after the samples passed through the crude oil layer. The pristine PET is almost entirely fouled by oil, so its transparency cannot be measured underwater. In contrast, the PAAm-coated HARn PET with the deep scratched surface (right) partially recovers its transparency and the shallow scratched surface (center) almost completely recovers its original transparency (see Movies S7 and S8). The underlying mechanism is similar to the recovery of transparency from the HARn PET to the PAAm-coated HARn PET. The space in the scratch that was filled by air is filled by water following submersion. The refractive index of water (n water ≈ 1.33 at 20 ℃) [50] is closer to the that of the PAAm hydrogel (n PAAm ≈ 1.51 at 20 ℃) [48] than to that of air(n air ≈ 1.00 at 20 ℃) [50], which reduces the light scattering effect.

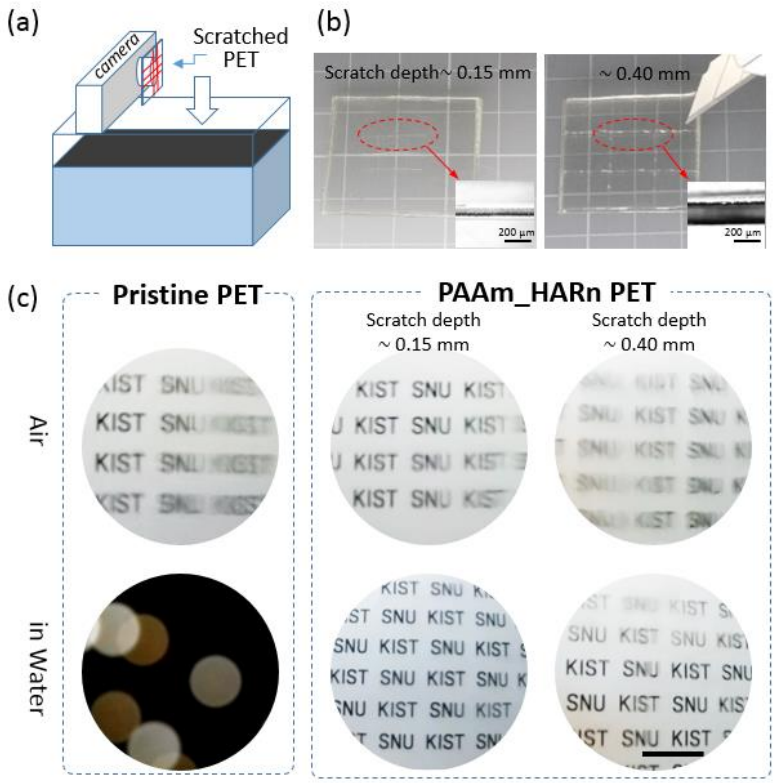

Fig. 3.13 Experiments on underwater camera protectors in crude-oil-covered water utilizing scratched PET surfaces. (a) Schematic of the immersion experiment. (b) Optical images of the PAAm-coated HARn PETs with different scratch depths of 0.15 (left) and 0.40 mm (right). The inset figures are optical microscope images of the scratches. (c) Optical images of the pristine and PAAm-coated HARn PET surfaces damaged by a razor blade. Shallow (depth ≈ 0.15 mm) and deep (depth ≈ 0.40 mm) scratches are formed on the PAAm-coated HARn PET surfaces. The upper row contains images captured before immersion and the lower row contains images captured after immersion. Scale bar is 10 mm.

3.4. Conclusions

We fabricated hydrogel-coated transparent PET film with strong interfacial adhesion utilizing HARns, which enhance wettability and optical transparency in oily water. One-step selective oxygen plasma etching was adopted to generate hydrophilicity and HARns on the PET. This approach induces strong interfacial adhesion, allowing the formation of mechanical interlocking hydrogel coating layer and PET substrate. Roughness and superhydrophilicity ensure the uniform deposition of a hydrogel solution, which penetrates to the bottom of the HARn structures to promote highly adhesive coating on the PET surface. The interfacial strength between the nanostructured PET and hydrogel was measured to be 11 times stronger than that between smooth PET and hydrogel. Transparency was also improved by the hydrogel coating on the nanostructured PET because the refractive indices of these materials are well matched. It was demonstrated that the anti-oil fouling properties of an underwater camera lens protected by the PAAm-coated HARn PET was robust in oily water, even following physical damage to the PET surface. The PAAm-coated HARn PET can be applied to various unmanned or manned underwater vehicles, optical sensors, and biological imaging equipment to provide protection from oil/lipid fouling.

3.5. References

[1] Xue, Z.; Cao, Y.; Liu, N.; Feng, L.; Jiang, L. Special wettable materials for oil/water separation. *Journal of Materials Chemistry A* **2014**, *2(8)*, 2445–2460.

[2] Chu, Z.; Seeger, S. Superamphiphobic surfaces. *Chemical Society Reviews* **2014**, *43(8)*, 2784–2798.

[3] Yao, X.; Gao, J.; Song, Y.; Jiang, L. Superoleophobic surfaces with controllable oil adhesion and their application in oil transportation. *Advanced Functional Materials* **2011**, *21(22)*, 4270–4276.

[4] Zhang, F.; Zhang, W. B.; Shi, Z.; Wang, D.; Jin, J.; Jiang, L. Nanowire-haired inorganic membranes with superhydrophilicity and underwater ultralow adhesive superoleophobicity for high-efficiency oil/water separation. *Advanced Materials* **2013**, *25(30)*, 4192–4198.

[5] Liu, X.; Gao, J.; Xue, Z.; Chen, L.; Lin, L.; Jiang, L.; Wang, S. Bioinspired oil strider floating at the oil/water interface supported by huge superoleophobic force. *ACS Nano* **2012**, *6(6)*, 5614–5620.

[6] Yong, J.; Chen, F.; Yang, Q.; Du, G.; Shan, C.; Bian, H.; Farooq, U.; Hou, X. Bioinspired transparent underwater superoleophobic and anti-oil surfaces. *Journal of Materials Chemistry A* **2015**, *3(18)*, 9379–9384.

[7] Akhtar, N.; Holm, V. R. A.; Thomas, P. J.; Svardal, B.; Askeland, S. H.; Holst, B. Underwater Superoleophobic Sapphire (0001) Surfaces. *The Journal of Physical Chemistry C* **2015**, *119(27)*, 15333–15338.

[8] Oberbillig, T.; Felde, N.; Franz, M.; Coriand, L.; Dahms, N.; Munderloh, K.; Schultz, K.; Fliedner, M.; Duparré, A. Oil-Repellent Optics for Wastewater Sensor Applications: A systematic combination of nano-roughness and adapted coatings. *Optik & Photonik* **2018**, *13(1)*, 14–18.

[9] Gu, Y.; Yang, J.; Zhou, S. A facile immersion-curing approach to surface-tailored poly(vinyl alcohol)/silica underwater superoleophobic coatings with improved transparency and robustness. *Journal of Materials Chemistry A* **2017**, *5(22)*, 10866–10875.

[10] Rezaei Kolahchi, A.; Ajji, A.; Carreau, P. J. Enhancing hydrophilicity of polyethylene terephthalate surface through melt blending. *Polymer Engineering & Science* **2015**, *55(2)*, 349–358.

[11] Liu, W.; Liu, X.; Fangteng, J.; Wang, S.; Fang, L.; Shen, H.; Xiang, S.; Sun, H.; Yang, B. Bioinspired polyethylene terephthalate nanocone arrays with underwater superoleophobicity and anti-bioadhesion properties. *Nanoscale* **2014**, *6(22)*, 13845–13853.

[12] Ko, T.-J.; Oh, K. H.; Moon, M.-W. Plasma-Induced Hetero-Nanostructures on a Polymer with Selective Metal Co-Deposition. *Advanced Materials Interfaces* **2015**, *2(1)*, 1400431.

[13] Schneider, H.; Niegisch, N.; Mennig, M.; Schmidt, H. Hydrophilic coating materials. In *Sol-Gel Technologies for Glass Producers and Users*, Springer: 2004, pp 187–194.

[14] Kim, S.; Bowen, R. A.; Zare, R. N. Transforming plastic surfaces with electrophilic backbones from hydrophobic to hydrophilic. *ACS Appl Mater Interfaces* **2015**, *7(3)*, 1925–1931.

[15] Inagaki, N. *Plasma Surface Modification and Plasma Polymerization*, Technomic Pub. Inc., Lancaster, PA, 1996.

[16] Murakami, T.; Kuroda, S.; Osawa, Z. Dynamics of polymeric solid surfaces treated with oxygen plasma: Effect of aging media after plasma treatment. *Journal of Colloid and Interface Science* **1998**, *202(1)*, 37–44.

[17] De Geyter, N.; Morent, R.; Leys, C. Influence of ambient conditions on the ageing behaviour of plasma-treated PET surfaces. *Nuclear Instruments and Methods in Physics Research Section B: Beam Interactions with Materials and Atoms* **2008**, *266(12–13)*, 3086–3090.

[18] Morra, M.; Occhiello, E.; Marola, R.; Garbassi, F.; Humphrey, P.; Johnson, D., On the Aging of Oxygen Plasma-Treated Polydimethylsiloxane Surfaces. *Journal of Colloid and Interface Science* **1990**, *137(1)*, 11–24.

[19] Occhiello, E.; Morra, M.; Morini, G.; Garbassi, F.; Humphrey, P. Oxygen-plasma-treated polypropylene interfaces with air, water, and epoxy resins: Part I. Air and water. *Journal of Applied Polymer Science* **1991**, *42(2)*, 551–559.

[20] Zhang, H.; Chiao, M. Anti-fouling coatings of poly (dimethylsiloxane) devices for biological and biomedical applications. *Journal of medical and biological engineering* **2015**, *35(2)*, 143–155.

[21] Chen, G.; Tang, W.; Wang, X.; Zhao, X.; Chen, C.; Zhu, Z. Applications of Hydrogels with Special Physical Properties in Biomedicine. *Polymers (Basel)* **2019**, *11(9)*.

[22] Sudre, G.; Olanier, L.; Tran, Y.; Hourdet, D.; Creton, C. Reversible adhesion between a hydrogel and a polymer brush. *Soft Matter* **2012**, *8(31)*, 8184.

[23] Xue, Z.; Wang, S.; Lin, L.; Chen, L.; Liu, M.; Feng, L.; Jiang, L. A novel superhydrophilic and underwater superoleophobic hydrogel-coated mesh for oil/water separation. *Adv Mater* **2011**, *23(37)*, 4270–4273.

[24] Yuk, H.; Zhang, T.; Lin, S.; Parada, G. A.; Zhao, X. Tough bonding of hydrogels to diverse non-porous surfaces. *Nat Mater* **2016**, *15(2)*, 190–196.

[25] Lorusso, E.; Ali, W.; Hildebrandt, M.; Mayer-Gall, T.; Gutmann, J. S. Hydrogel Functionalized Polyester Fabrics by UV-Induced Photopolymerization. *Polymers (Basel)* **2019**, *11(8)*.

[26] Yang, J.; Bai, R.; Chen, B.; Suo, Z., Hydrogel Adhesion: A Supramolecular Synergy of Chemistry, Topology, and Mechanics. Advanced Functional Materials **2019**, 1901693.

[27] Wang, X.; Fang, D.; Yoon, K.; Hsiao, B. S.; Chu, B. High performance ultrafiltration composite membranes based on poly (vinyl alcohol) hydrogel coating on crosslinked nanofibrous poly (vinyl alcohol) scaffold. *Journal of Membrane Science* **2006**, *278(1–2)*, 261–268.

[28] Kurokawa, T.; Furukawa, H.; Wang, W.; Tanaka, Y.; Gong, J. P. Formation of a strong hydrogel-porous solid interface via the double-network principle. *Acta Biomater* **2010**, *6(4)*, 1353–1359.

[29] Phan, L. T.; Yoon, S. M.; Moon, M. W. Plasma-Based Nanostructuring of Polymers: A Review. *Polymers (Basel)* **2017**, *9(9)*.

[30] Li, W.; Liu, X.; Deng, Z.; Chen, Y.; Yu, Q.; Tang, W.; Sun, T. L.; Zhang, Y. S.; Yue, K. Tough Bonding, On-Demand Debonding, and Facile Rebonding between Hydrogels and Diverse Metal Surfaces. *Adv Mater* **2019**, *e1904732*.

[31] Gwon, S. H.; Oh, J. H.; Kim, M.; Choi, S.; Oh, K. H.; Sun, J. Y. Sewable soft shields for the gamma-ray radiation. *Sci Rep* **2018**, *8(1)*, 1852.

[32] Shin, B.; Moon, M. W.; Kim, H. Y. Rings, igloos, and pebbles of salt formed by drying saline drops. *Langmuir* **2014**, *30(43)*, 12837–12842.

[33] Oh, J.-H.; Ko, T.-J.; Moon, M.-W.; Park, C. H. Nanostructured fabric with robust superhydrophobicity induced by a thermal hydrophobic ageing process. *RSC Advances* **2017**, *7(41)*, 25597–25604.

[34] Her, E.; Ko, T. J.; Shin, B.; Roh, H.; Dai, W.; Seong, W.; Kim, H. Y.; Lee, K. R.; Oh, K.; Moon, M. W. Superhydrophobic transparent surface of nanostructured poly (methyl methacrylate) enhanced by a hydrolysis reaction. *Plasma Processes and Polymers* **2013**, *10(5)*, 481–488.

[35] Grover, C. N.; Gwynne, J. H.; Pugh, N.; Hamaia, S.; Farndale, R. W.; Best, S. M.; Cameron, R. E. Crosslinking and composition influence the

surface properties, mechanical stiffness and cell reactivity of collagen-based films. *Acta Biomater* **2012**, *8(8)*, 3080–3090.

[36] Feng, X.; Feng, L.; Jin, M.; Zhai, J.; Jiang, L.; Zhu, D. Reversible super-hydrophobicity to super-hydrophilicity transition of aligned ZnO nanorod films. *Journal of the American Chemical Society* **2004**, *126(1)*, 62–63.

[37] Gao, S.; Sun, J.; Liu, P.; Zhang, F.; Zhang, W.; Yuan, S.; Li, J.; Jin, J. A Robust Polyionized Hydrogel with an Unprecedented Underwater Anti-Crude-Oil-Adhesion Property. *Adv Mater* **2016**, *28(26)*, 5307–5314.

[38] Schutzius, T. M.; Jung, S.; Maitra, T.; Graeber, G.; Köhme, M.; Poulikakos, D. Spontaneous droplet trampolining on rigid superhydrophobic surfaces. *Nature* **2015**, *527(7576)*, 82.

[39] Li, Y.; Lei, M. Nanotexturing and wettability ageing of polypropylene surfaces modified by oxygen capacitively coupled radio frequency plasma. *Journal of Materials Science & Technology* **2014**, *30(10)*, 965–972.

[40] Quéré, D. Wetting and roughness. *Annu. Rev. Mater. Res.* **2008**, *38*, 71–99.

[41] Neumann, A.; Good, R. Thermodynamics of contact angles. I. Heterogeneous solid surfaces. *Journal of Colloid and Interface Science* **1972**, *38(2)*, 341–358.

[42] El-Anwar, I.; El-Nabawy, O.; El-Hennwii, S.; Salama, A. Dielectric properties of polyacrylamide and its utilization as a hydrogel. *Chaos, Solitons & Fractals* **2000**, *11(8)*, 1303–1311.

[43] Natkański, P.; Kuśtrowski, P.; Białas, A.; Piwowarska, Z.; Michalik, M. Thermal stability of montmorillonite polyacrylamide and polyacrylate nanocomposites and adsorption of Fe(III) ions. *Applied Clay Science* **2013**, *75–76*, 153–157.

[44] Kendall, K. Thin-film peeling-the elastic term. *Journal of Physics D: Applied Physics* **1975**, *8(13)*, 1449.

[45] Liu, J.; Yang, C.; Yin, T.; Wang, Z.; Qu, S.; Suo, Z. Polyacrylamide hydrogels. II. elastic dissipater. *Journal of the Mechanics and Physics of Solids* **2019**, *133*, 103737.

[46] Liu, X.; Zhang, Q.; Gao, G. Bioinspired Adhesive Hydrogels Tackified by Nucleobases. *Advanced Functional Materials* **2017**, *27(44)*, 1703132.

[47] Cai, G.; Wang, J.; Eh, A. L.-S.; Chen, J.; Qian, K.; Xiong, J.; Thangavel, G.; Lee, P. S. Diphylleia grayi-Inspired Stretchable Hydrochromics with Large Optical Modulation in the Visible–Near-Infrared Region. *ACS applied materials & interfaces* **2018**, *10(43)*, 37685–37693.

[48] Aouada, F. A.; de Moura, M. R.; Fernandes, P. R. G.; Rubira, A. F.; Muniz, E. C. Optical and morphological characterization of polyacrylamide hydrogel and liquid crystal systems. *European Polymer Journal* **2005**, *41(9)*, 2134–2141.

[49] Yang, S. M.; Hong, S.; Kim, S. Y. Optical, mechanical, and photoelastic anisotropy of biaxially stretched polyethylene terephthalate films studied

using transmission ellipsometer equipped with strain camera and stress gauge. *Journal of Polymer Science Part B: Polymer Physics* **2019**, *57(3)*, 152–160.

[50] Hecht, E. *Optics*. Pearson: 2015.

Chapter 4. Anti-Mineral fouling

4.1. Introduction

In recent decades, oil is the most important energy source in the world, and is expected to remain in that position for the next decades. The oil production, consumption and transportation are increasing every year. And the oil spill risk also increases as the oil transportation and handling volumes of oil are increase. [1] As a result, recent studies focus on the oil spill management technologies which is oil-water separation to respond the trend and irregular accidents. To respond the oil spill accident, many studies focus on this topic. The water-removing-type (e.g. oil-water separation filters) using hydrophilic material has been intensively studied than the oil-removing-type (e.g. oil absorbents) using hydrophobic material due to the advantages of oil-water separation efficiency and recyclability. [2] However, there are few cases applicate to the oil spill managements, and many researches are still being reported at the laboratory level, because of it would not represents real harsh environments conditions.

The most oil spill had been took place on the sea, and the verification is required at the sea environment for the oil respond equipment. The dissolved minerals which are salt (Sodium Chloride) and other minerals in the sea water, it will precipitated on the operated equipment or membrane as sea water evaporate and the crystallization can physical damage to the surface. The fouled or precipitated mineral crystals can easily remove by water cleaning or immersion at the sea, however, the damaged surface of membrane especially functional surface

using coating or enhance roughness, was decreased the capacity of oil-water separation. It is hard to recovery of capacity and should be replace and reduce the work efficiency.

When the evaporation front is in the porous medium, salt crystals will precipitate inside the porous medium if the solution becomes supersaturated; this is called subflorescence. When the liquid vapor interface remains at the porous medium surface, supersaturation leads to precipitation at the surface or efflorescence. [3, 4] Salt crystallization is a critical issue in deterioration of building structure, marble status and fresco. (Fig. 4.1) [5]

❖ **Enhance the surface roughness**

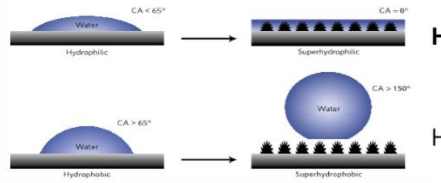

Hydrophilic + Roughness → Superhydrophilic

Hydrophobic + Roughness → Superhydrophobic

Tian et al., *Nat. Mater.*, **12** (2013)

❖ **Salt damage of porous surface**

Fresco painting, Italy

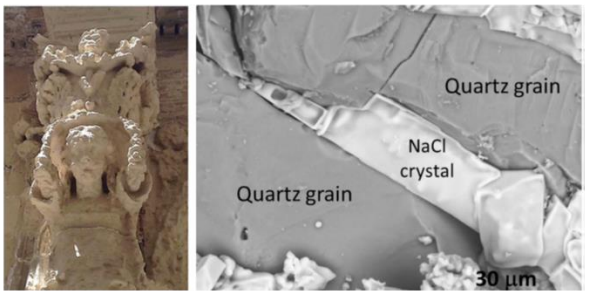

J. Desarnaud et al . Scientific Reports volume6, 30856 (2016)

Fig. 4.1 Function of surface enhancement via roughness increasing and case of salt damage that are fresco painting or status.

Due to the intrinsic nature of the material, the hydrophilic material has more risk of subflorescence than the hydrophobic material. Water-removing type membranes, which are currently being studied extensively, also have more risk by salt damage. Salt damage makes it difficult to use in the sea environment for water-removing type which mainly use hydrophilic materials, compared to the oil-removing type, mainly uses hydrophobic materials which water is not easy to get into the structure. In particular, the surfaces that maximize their functionality by increase of surface roughness, [6] increase the amount of space that can be penetrated by sea water, and increase the risk of salt damage.

Here, we have propose a high-aspect-ratio (HAR) nanostructure that can overcome the salt damage. The uniform and dense HAR nano-pillars fabricated on the commercial cotton fabric, controls the salt precipitated location where is top of the nano-pillar not a between or bottom of nano-pillars. And we conduct the experiment and model establishment to analysis and verification.

4.2. Method

The woven cotton fabric was purchased from the commercial company (Namyang fabric, South Korea). The samples were prepared for 2.5 cm × 2.5 cm in size. The HAR nanostructures were fabricated via O2 plasma etching on the cotton fibers using a custom-built plasma etching device under the plasma power and substrate bias voltage set for 230 W and 400 V, respectively. With the oxygen

gas flow rate of 100 sccm, the plasma treatment duration was performed for 10min, resulting in the ARs, 18.4. Surface morphology was explored by a scanning electron microscope (SEM, Inspect-F, FEI, USA). A 6 nm thick Pt film was covered onto the fabrics to provide better conductivity and prevent generating electron charge on the polymeric fabric. The SEM electron accelerating voltage was 7 kV. A contact angle (CA) of oil was measured underwater condition for the light crude oil of 0.87 g/ml in density (Hyundai Oil Bank Co., South Korea) droplets with a volume of 10.0 ± 0.5 μl. Water immersion test was performed on various fabrics recorded with a digital camera having the resolution of 15 megapixel (Canon EOS 60D).

The 0.5 M sodium chloride solution which is similar concentration of average sea water(ref,) was purchased from a commercial company (Daejung Chemical Co. South Korea)

4.3. Experiment

4.3.1. Increase of surface roughness using O2 plasma treatment

The increase of nano/micro scales of surface roughness can enhance the material's intrinsic hydrophilicity and hydrophobicity. [7] Here, we demonstrated the robustness of hydrophilicity even the intrinsic property of substrate was hydrophobicity. We prepared diverse fabrics which are cellulose (cotton), PET, PP, PE and PTFE. The cellulose is representatively hydrophilic material and the other

materials have hydrophobic property. These samples were oxygen plasma treatment as duration time increase. The surface morphology investigated by SEM. Fig. 4.2 shows evolution of surface morphology that's roughness was increased as plasma duration time increase.

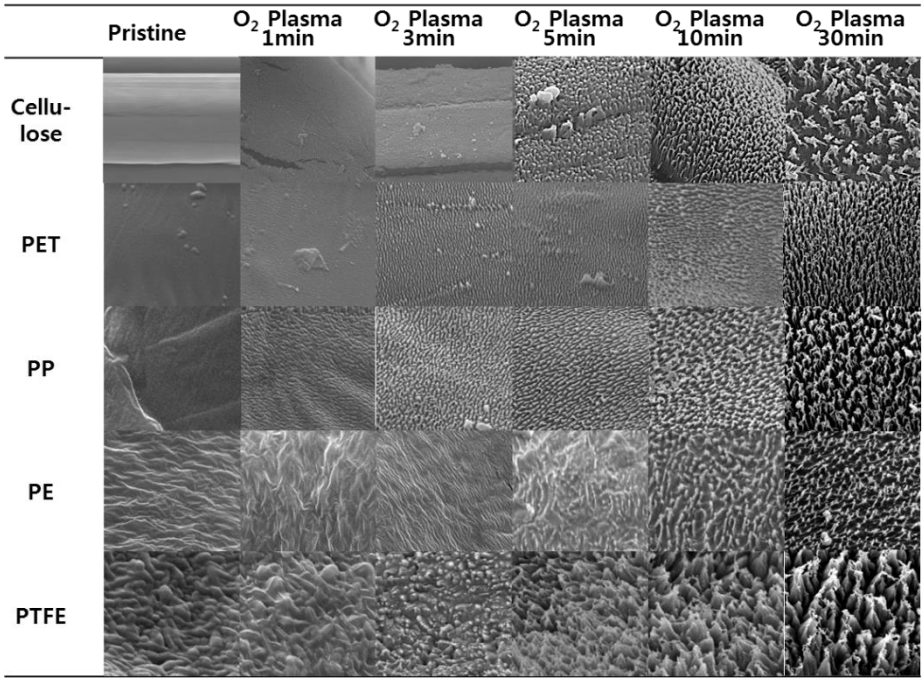

Fig. 4.2 Evolution of surface roughness as O_2 plasma duration change. Diverse materials were fabricated from intrinsic hydrophilic (cellulose) to hydrophobic (PET, PP, PE and PTFE). The roughness of surfaces increase as duration time increase.

4.3.2. Robustness of hydrophilicity and underwater oleophobicity

To investigate the result of fabricated samples' hydrophilicity and underwater oleophobicity, we conducted measurement of water contact angles (WCA) and underwater oil contact angles (OCA). Fig. 4.3(a) shows WCA of each material cellulose fabric has a high hydrophilicity regardless oxygen plasma treatment duration. On the other hands, pristine PET, PP, PE and PTFE show hydrophobicity, the WCAs are more than 117.5° each substrate. As oxygen plasma treatment duration increase, PET, PP and PE substrates were converse to hydrophilic property except PTFE.

Fig. 4.3(b) shows underwater oleophobicity of each substrate as oxygen duration increase that's trend was similar with hydrophobicity.(Fig. 4.3(a)) The measured OCAs plotted with each case and the OCAs were dramatically increase after oxygen plasma treatment. Additionally the indicator of adhesion to the substrate, contact angle hysteresis (CAH) also dramatically decrease after oxygen plasma treatment except PTFE.

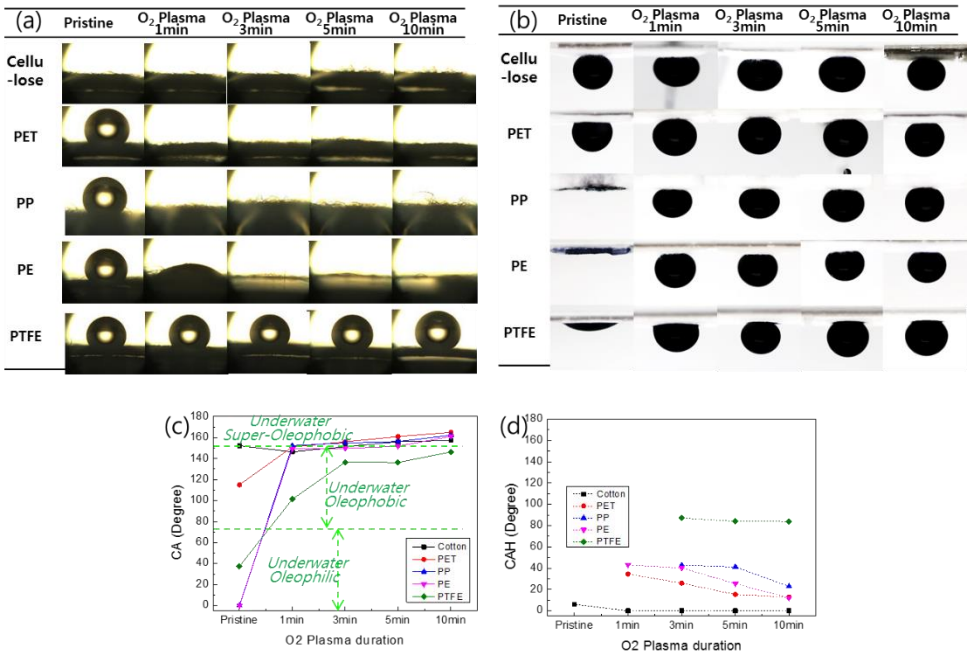

Fig. 4.3 (a) Evaluation of hydrophilicity via water contact angle(CA) measurement in air. Water CAs were dramatically decreased after O2 plasma treatment except PTFE. (b) Evaluation of underwater oleophobicity via underwater oil contact angle. Underwater oil CAs were dramatically increased. (c) Underwater oil contact angle(CA) and contact angle hysteresis(CAH) traced with O2 plasma duration.

4.3.3. Hydrophilic/hydrophobic surface's water wet behavior

In order to investigate the behavior of the nanostructures of the hydrophilic surface when it was immersed in water, we observed the hydrophilic and hydrophobic HAR nanostructures' morphologies after dry as shown in Fig 4.4 First column is the surface before water wet (a, c). Second column is the dried surface after water wet (b, d). Hydrophilic nano-pillars were aggregated after water contact and dried (b). On the other hands, hydrophobic nano-pillars were not aggregated even water immersed (d). As shown in Fig. 4.4b, the hydrophilic nano-pillar was aggregated when water totally immersed its structures as water evaporate. [8] However, Fig. 4.4d, the hydrophobic nano-pillar was not aggregated in spite of being immersed by water.

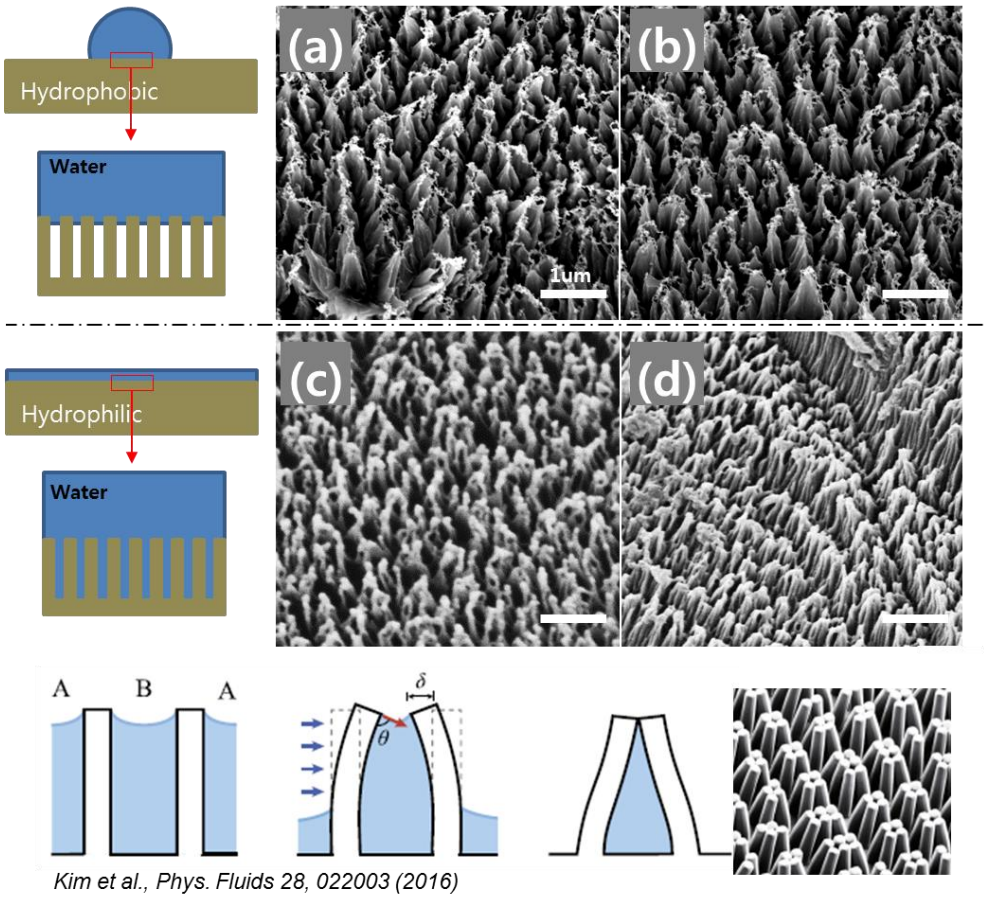

Fig. 4.4 High-aspect-ratio nanostructure induced PTFE (hydrophobic, upper row) and, Cotton (hydrophilic lower row). First column is the surface before water wet (a, c). Second column is the dried surface after water wet(b, d). Hydrophobic nano-pillars were not aggregated even water immersed (b). On the other hands, hydrophilic nano-pillars were aggregated after water contact and dried (d). Each scale bar is 1um.

4.3.4. NaCl precipitation behavior on the hydrophilic/hydrophobic nanostructures.

Polyethylene terephthalate (PET), intrinsic hydrophobic property, was prepared under 30min treatment condition by choosing the oxygen plasma treatment that induce the hydrophilic high-aspect-ratio (HAR) nanostructures surface. Right after the treatment (hydrophilic property was induced by OH functional groups were implemented), the HAR PET surfaces was fouled by 10 μl 0.5M salt solution in an air environment, and placed on the room temperature during 24hr. Additionally, right after the oxygen plasma treatment, the PET sample was aged to recover the intrinsic hydrophobicity during 24h. After the aging process, the hydrophobic HAR PET was fouled by 0.5M salt solution under same condition of hydrophilic PET.

The salt precipitated either surfaces were investigated by SEM and Focused Ion Beam (FIB) cross section. Fig. 4.5 shows salt precipitation behavior each surface condition. The salt was placed like coin shape on the hydrophobic surface. In contrast, the salt crystals were spread out on the hydrophilic surface. In particularly, the salt crystals were precipitated on the HAR nanostructures that were completely immersed by salt solution. (Fig. 4.4d)

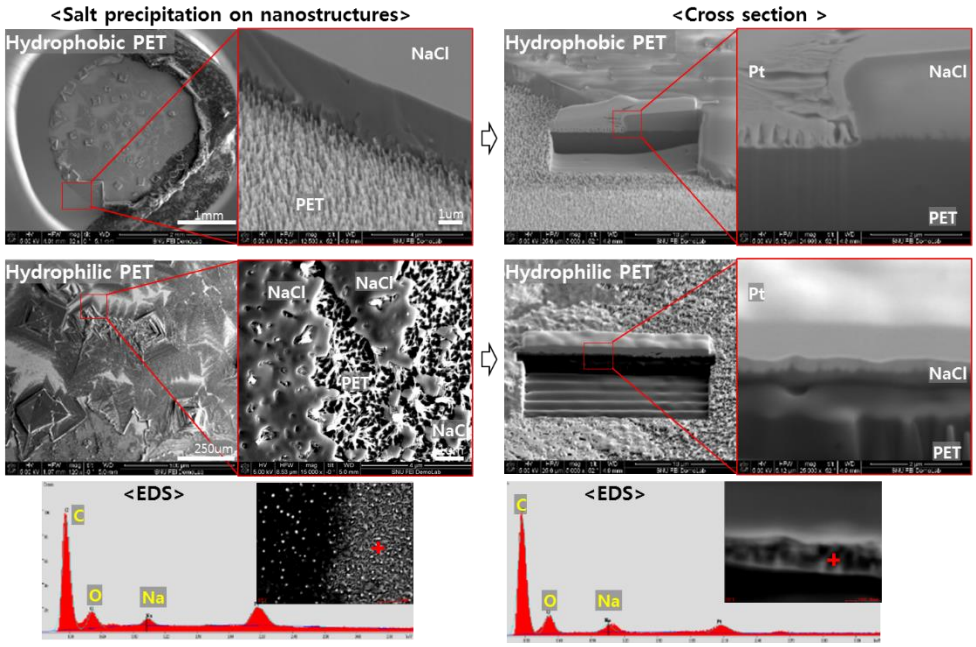

Fig. 4.5 Salt precipitated behavior on the hydrophobic/hydrophilic surface. The salt precipitated on the hydrophilic nano-pillars even though the salt solution completely penetrate each structures.

4.3.5. Salt precipitation on the hydrophilic surface

Hydrophilic HAR nanostructured samples were immersed in a 0.5M salt solution, similar to the average concentration of seawater [9] and observed after dried to verify the damage of the surface. The nanostructures were aggregated after water immersion.(Fig. 4.6(a)) Fig. 4.6(b) shows the precipitation of salt crystals on the top of the nanostructure after the immersion experiment, and Fig. 4.6b is the salt precipitated at the top of the HAR structure after dipping in salt water. Fig. 4.6(c) shows the nanostructures after water washing the salt precipitated surface, and it was observed that there was no difference between before and after the salt precipitation, and the nanostructures were not damaged even after the salt precipitation. Fig. 4.6(d) shows the measurement of contact angle (CA) and contact angle hysteresis (CAH) of each sample pristine, wet surface (a) and salt precipitated surface (c). There was no capacity difference of underwater oleophobicity of each condition before and after salt precipitation on the HAR nanostructures.

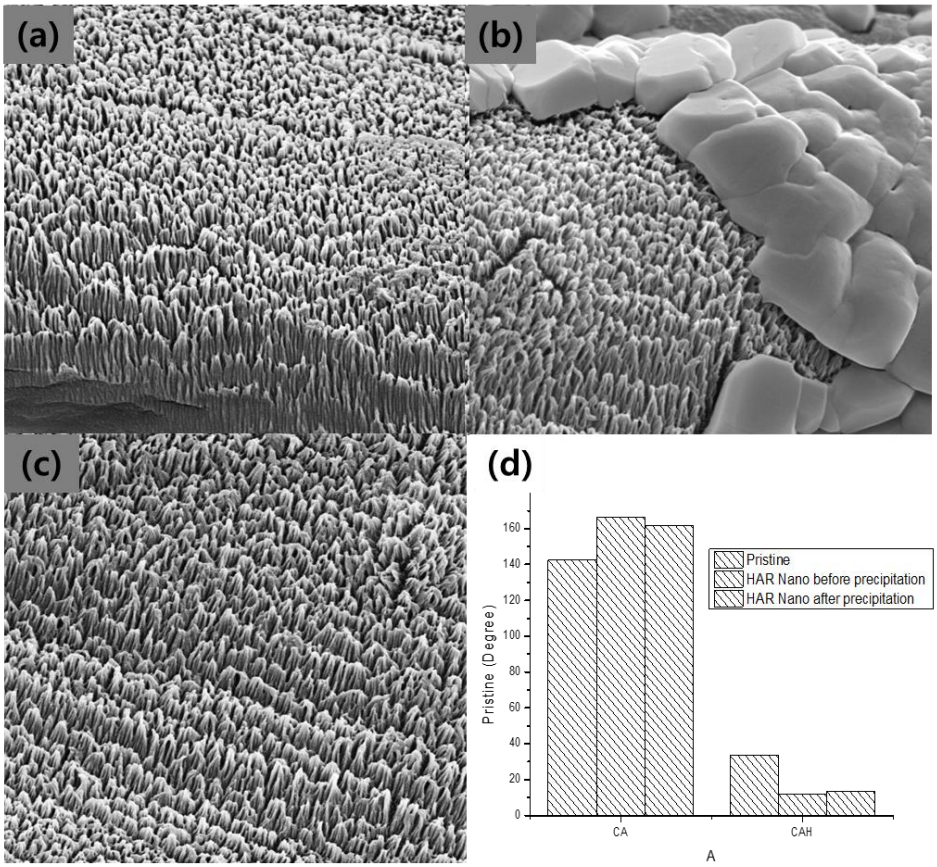

Fig. 4.6 High-aspect-ratio nanostructure induced on the Cotton fiber. (a) The aggregated nano-pillars after water wet. (b) The precipitated salt on the nano-pillar not between. (c) The dried surface after salt precipitated and water cleaning. The nano-pillars were not damaged just aggregated like (a) even the salt precipitated on the surface. (d) The measurement of contact angle and contact angle hysteresis of each sample pristine, wet surface (a) and salt precipitated surface (c). Each scale bar is 300nm.

4.4. Salt precipitation analysis

4.4.1. System description

Concentration of salt solution at surface is increase as water evaporation. NaCl ion diffusion starts. (Fig 4.7(a)) Nucleation at saturation point (≈6.12M/kg) The surface of solution reaches the saturation point first, but the nucleation is inhibited owing to the homogeneous nucleation. (Fig. 4.7(b))

With a high probability, Heterogeneous nucleation starts at top of nano-pillars owing to the NaCl diffusion and evaporation continuing. (Fig. 4.7(b)) If the diffusion rate is low near top of the nano-pillars, NaCl likely nucleates at the top of pillar rather than into nano-pillars(Fig. 4.7(c)) Even if the NaCl nucleates between or low part of nano-pillar, the Gibbs-Thomson effect inhibits nucleation and growth.

When the solution level drops below the height of the nano-pillars, capillary force stimulates efflorescence phenomenon due to the porous structure. (Fig. 4.7(d))

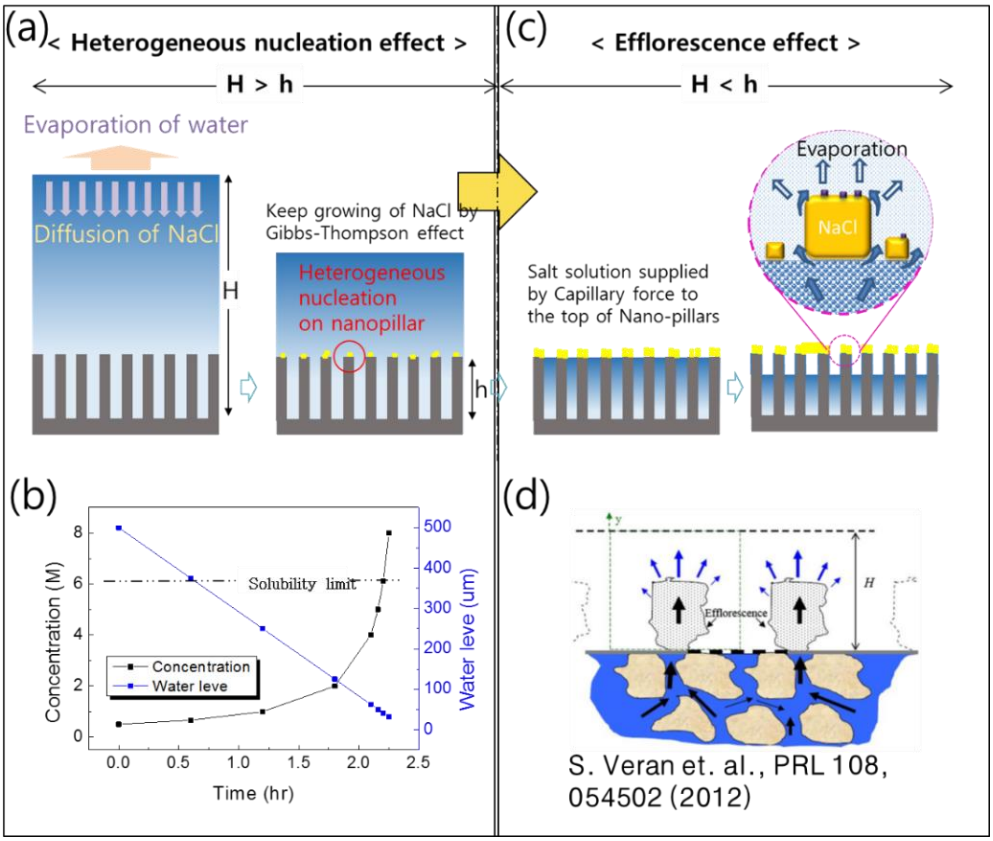

Fig. 4.7 The schematic of salt precipitation on the hydrophilic HAR nanostructures (a) Concentration of solution at surface (0.5M, average seawater concentration) is increase as water evaporation. NaCl ion diffusion starts and reaching saturation point.(≈6.12M/kg) The surface of solution reaches the saturation point first, but the nucleation is inhibited owing to the homogeneous nucleation. With a high probability, Heterogeneous nucleation starts at top of nano-pillars owing to the NaCl diffusion and evaporation continuing. Even if the NaCl nucleates between or low part of nano-pillar, the Gibbs-Thomson effect inhibits nucleation and growth. The diffusion rate is much faster than evaporation rate. (b) The saturation concentration reached before the solution level reach to the top of the

nanostructures (h ≈ 2um) if the initial solution level(H) more than 24.48um. (c) When the solution level drops below the height of the nano-pillars, capillary force stimulates efflorescence phenomenon due to the porous structure. (d) The schematic of efflorescence effect

4.4.2. Salt solution evaporation and diffusion under efflorescence principle

The variables of water evaporation and salt ion transportation under efflorescence principle were established as follow. (Fig. 4.8)

NaCl solution transported to the Nano pillar by capillary force

Water evaporates each site

- 2’ : Evaporation rate (J1) > 0

- 2” : Evaporation rate (J2_mean) ≈ 0

∵ J2_mean = Jd_vapor/(b+2c) ≈ negligible

※ J2_max × (b+2c) > Jd_vapor

(J1 = J2_max)

* Jd_vapor : Vaper diffusion rate ?

NaCl Solution becomes the crystallization concentration

- Co = wn / ww

where, Co : initial concentration,

w : weight(or mol?) of nacl and water

- C(t)1 = wn / (ww − J1×t) → Csat

C(t)2 = wn / (ww − J2×t) ≈ Co

∴ NaCl precipitates at 2’ continuously

Go to step ①

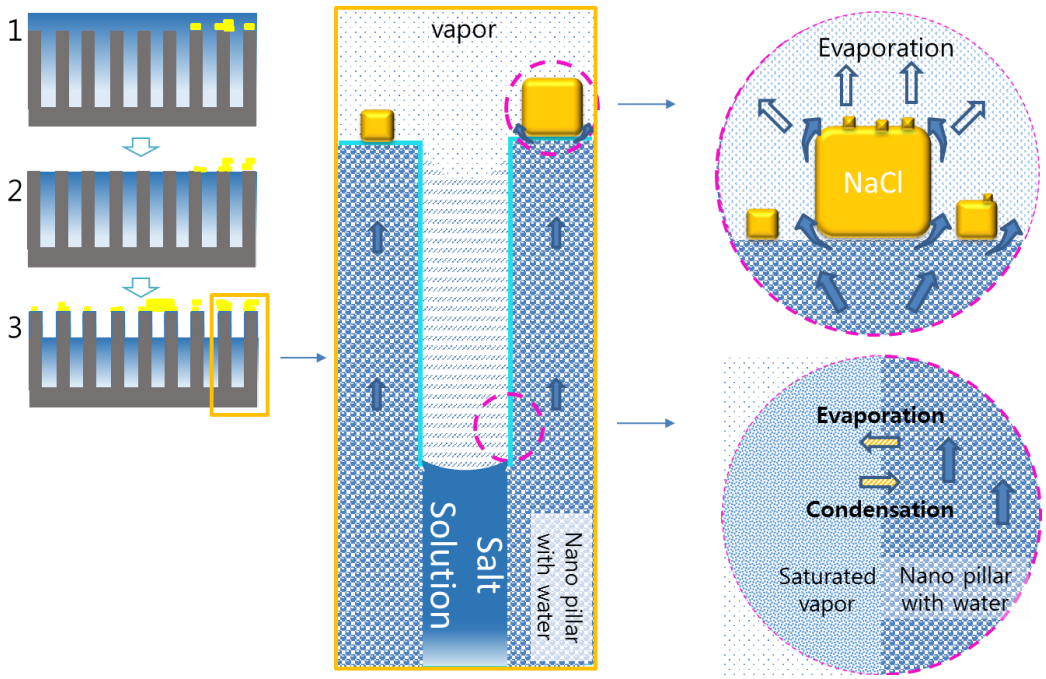

Fig. 4.8 Salt crystal growth on the nano-pillar as water evaporation which is phenomenon of efflorescence.

4.5. Conclusion

In this study, we introduce the mineral precipitation control using high - aspect-ratio (HAR) nanostructures, inspired by plants water-mineral transportation mechanism. These are explained from experiments and model analysis with simple efflorescence model, that HAR nanostructures does not damage from the mineral crystallization even the hydrophilic nano-pillars were totally immersed in seawater. We also demonstrate robustness of underwater superoleophobicity by controlled the HAR.

4.6. Reference

[1] Oil Tanker Spill Statistics 2017. ITOPF, 16, (2018).

[2] Xue, Z., Cao, Y., Liu, N., Feng, L. & Jiang, L. Special wettable materials for oil/water separation. J. Mater. Chem. A, 2(8), 2445-2460, (2014).

[3] S. Veran., M. Marcoux, and M. Prat, Discrete Salt Crystallization at the Surface of a Porous Medium, PHYSICAL REVIEW LETTERS, PRL 108, 054502 (2012)

[4] Mansoureh N., Nima S., and Muhammad S., Pore-scale dynamics of salt precipitation in drying porous media, PHYSICAL REVIEW E 88, 032404 (2013)

[5] J. Desarnaud, and Bonn N., The Pressure induced by salt crystallization in confinement, Scientific Reports volume 6, Article number: 30856 (2016)

[6] Liu, M., Wang, S. & Jiang, L. Nature-inspired superwettability systems. Nat. Rev. Mater., 2(7), 17036, (2017).

[7] Ye T., and Lei J., Intrinsically robust hydrophobicity,NATURE MATERIALS | VOL 12 | APRIL 2013

[8] T.H. Kim, J.C. Kim and H.Y. Kim, Evaporation-driven clustering of microscale pillars and lamellae, PHYSICS OF FLUIDS 28, 022003 (2016)

[9] Kim, D. H. et al. UV-responsive nano-sponge for oil absorption and desorption. Sci Rep, 5, 12908 (2015).

Abstract in Korean

자연의 많은 생물들은 기능성 표면을 가지고 주변환경에 적응하며 생존해 나가고 있다. 이들의 표면을 자세히 들여다 보면, 미세하게 거친 표면을 가진 것을 확인할 수 있다. 이런 거칠기를 가진 표면은 친수 또는 소수 표면을 구현하는데 중요한 역할을 하는 것이 밝혀져 있으며, 많은 연구자들에게 영감을 주고 있다. 그래서 우리는 이 개념을 바탕으로 많은 도전적인 주제들이 있는 방유성(anti-oil fouling), 자가세정(self-cleaning), 그리고, 김 서림 방지(anti-fogging) 등의 연구분야에서 해결책을 제시하고자 하였다.

첫 장에서는 나노구조를 가진 셀룰로오스 섬유와 공기방울을 이용해서 건조상태에서 기름에 오염되어도 쉽게 물로 세척하는 기술을 연구하였다. 나노구조가 생성된 섬유와 다공성 구조 특성의 두 가지 기능을 활용하여, 건조상태에서 기름에 오염된 표면을 세척하는 기술이다. 고종횡비 (high-aspect-ratio) 나노구조가 생성된 표면은 기름과 맞닿는 표면의 면적을 줄이고, 물에 의한 기름의 세척력을 증대시킨다. 다공성 구조의 섬유는 많은 공기를 함유하고 있어서 기름에 오염된 후 물에 의해 세척 시 배압(backpressure)과 부력을 작용시켜서 오염된 표면에서 기름의 탈락을 가속시킨다. 이 원리를 기반으로 초친수 경향을 갖는 셀룰로오스 기반의 레이온 섬유에 선택적 산소 플라즈마 에칭을 통해서 고종횡비의 나노 구조를 생성 시키고, 기름에 오염된 표면을 다양한 방법으로 검증하여 최적의 성능을 제시한다. 또한, 수중 센서의 기름오염을 방지할 수 있는 센서 보호막의 시연을 통해서, 유수분리뿐만 아니라, 수중 UAV 등의 분야에 적용할 수 있는 가능성을

제시하였다.

두 번째 장에서는, 첫 번째 장에서 연구한 내용을 더욱 개선하여 투명하면서도 방유성을 갖는 합성 폴리머 표면을 연구하였다. 기존의 합성 폴리머는 고유의 친유성 (oleophilic) 으로 인하여, 기름에 쉽게 오염되어 수중 카메라나, 수중 광학센서의 렌즈로 사용할 수 없었다. 그래서 대부분의 수중 방유성(anti-oil fouling)을 갖는 소재는 유리와 같은 세라믹 소재에서 집중적으로 연구되었다. 이에 우리는 선택적 산소 플라즈마 에칭 기법을 통하여, 폴리머 (PET) 표면의 화학적 특성을 통제하고, 나아가서 일반적으로 매끄러운 표면인 투명한 표면에 코팅을 효과적으로 할 수 있도록, 고종횡비의 나노구조를 형성시킨 후 하이드로젤 코팅을 통해서 이 난관을 극복하였다. 이를 통해서 수중 카메라에 적용하여 기름이 유출된 물에서도 기름의 오염 걱정 없이 사용할 수 있는 기술을 시연하였다.

세 번째 장에서는, 대부분의 기름이 유출되는 바다환경에서의 고종횡비 나노 구조의 방유성을 검증하기 위한 연구를 진행하였다. 바닷물은 다량의 미네랄과 불순물을 함유하고 있어서, 해양환경에서 작업 후에 담수 세척 없이 보관 시에 소금과 같은 미네랄의 석출을 동반한다. 이때 석출되는 미네랄은 나노구조를 가진 표면에 손상을 가하여, 방유성 등의 기능저하를 야기할 수 있다. 이에 우리는 나노구조에서 미네랄의 석출 거동에 대한 실험과 모델링으로 검증하여, 손상 없는 결과와 원리를 규명하였다.

핵심어 : 친수성, 방유성, 미네럴 내성, 나노구조, 산소 플라즈마, 수중 방유성, 하이드로젤

학번 : 2016-30194